Available online at www.sciencedirect.com
SCIENCE DIRECT®
Physics of the Earth and Planetary Interiors 149 (2005) 279–306
PHYSICS OF THE EARTH AND PLANETARY INTERIORS
www.elsevier.com/locate/pepi

Thermal expansivity and elastic properties of the lithospheric mantle: results from mineral physics of composites

Juan Carlos Afonso[a,*], Giorgio Ranalli[a], Manel Fernàndez[b]

[a] *Department of Earth Sciences and Ottawa-Carleton Geoscience Centre, Carleton University, 1125 Colonel By Drive, Ottawa, Canada K1S 5B6*
[b] *Institute of Earth Sciences "J. Almera", C.S.I.C., Luís Solé Sabarís s/n, 08028 Barcelona, Spain*

Received 20 April 2004; received in revised form 18 October 2004; accepted 18 October 2004

Abstract

The elastic properties and the coefficient of thermal expansion (CTE) of the lithospheric mantle are important parameters that affect the results of lithospheric modelling. However, there is still no consensus on which values are the most appropriate to model the lithosphere, and various average values are used for lithospheres of different age, thermal state, and composition. We present an integrated approach to calculate the elastic properties and the CTE of mantle rocks, based on the mineral physics of composites and considering the spatial heterogeneity of the lithospheric mantle. The method considers the dependence of parameters on pressure and temperature, following a procedure based on an extension of the shear-lag model and thermal expansivity systematics.

Representative values are calculated for three lithospheric domains: (a) Archean lithosphere, (b) Phanerozoic continental lithosphere, and (c) oceanic lithosphere. For the case of Archean lithosphere, values of CTE between (3.04 and 3.11) $\times 10^{-5}\,K^{-1}$ are found to be suitable for modelling, and a constant depth-derivative for P-waves $\partial V_p/\partial z \sim 2.30 \times 10^{-3}\,s^{-1}$ is estimated. Results for Phanerozoic lithosphere show that no single average value of CTE can be used in modelling. Values range non-linearly between (3.25 and 3.47) $\times 10^{-5}\,K^{-1}$ at pressures equivalent to depths of 25 and 100 km, respectively. The P-wave velocity variation with depth exhibits a decrease in the range of 25–40 km, followed by almost a constant value of $\sim$8.08 km s^{-1} between 40 and 60 km, and a systematic increase with a depth-derivative $\partial V_p/\partial z \sim 1.12 \times 10^{-3}\,s^{-1}$ from 60 km downwards. The variation in the CTE is largest in oceanic lithosphere. In young plates ($\lesssim$20 Ma), values of the CTE range non-linearly from (3.25 to 3.82) $\times 10^{-5}\,K^{-1}$ at pressures equivalent to depths of 10 and 50 km, respectively. In old oceanic lithosphere ($\sim$100 Ma), the CTE is slightly smaller, showing values in the range of (3.0–3.7) $\times 10^{-5}\,K^{-1}$ at 10 and 80 km, respectively, giving a typical average value of $\sim 3.45 \times 10^{-5}\,K^{-1}$. P-wave velocity in young oceanic lithosphere decreases from $\sim$8.14 to 8.0 km s^{-1} in the first 30 km, then follows a nearly constant path downwards. In old oceanic lithosphere, on the other hand, a systematic reduction from $\sim$8.2 to 8.1 km s^{-1} in P-wave velocities is predicted as depth increases from 10 to 80 km.

The effects of heterogeneities in CTE and elastic parameters are particularly noticeable in Archean lithosphere, where difference in predicted elevations and geoid heights can reach values of $\geq$300 and $\sim$6 m, respectively, when compared to standard models.

* Corresponding author. Tel.: +1 613 5202600x4392; fax: +1 613 5202569.
E-mail addresses: jcarlos@ccs.carleton.ca (J.C. Afonso), granalli@ccs.carleton.ca (G. Ranalli), mfernandez@ija.csic.es (M. Fernàndez).

0031-9201/$ – see front matter
doi:10.1016/j.pepi.2004.10.003

These effects are less ($\lesssim$40 and 0.25 m, respectively) in Phanerozoic continental and oceanic lithospheres. Uncertainties in experimental data and geotherms indicate that compositional effects cannot be completely resolved by seismic tomography in regions with P-wave and S-wave anomalies $\lesssim\pm1.5$ and $\pm3\%$, respectively.

Keywords: Lithospheric mantle; Elastic properties; Thermal expansivity; Mineral physics; Lithospheric modelling

1. Introduction

Lithospheric modelling provides critical information for understanding the dynamics of plate tectonics. The main goal is to obtain a model of the thermal, mechanical, and structural characteristics of the lithosphere, which in turn gives insights about geodynamic processes such as subduction, delamination, rifting, etc. The lithospheric mantle plays a major role in determining the total strength, buoyancy and thickness of the lithospheric plate. Several methodologies have been proposed, all of them making use of regional geophysical observables as constraints to the model. Half-space and plate cooling thermal models predict a $t^{1/2}$ dependence of the ocean-floor topography and heat flow, where t is age, as well as a progressive decrease of the geoid and deflection of isotherms away from the oceanic ridge (e.g. Parsons and Sclater, 1977; Stein and Stein, 1992; Schubert et al., 2001). The continental lithosphere behaves in a more complex way than the oceanic lithosphere, due in part to the presence of a relatively thick and heterogeneous continental crust, and its thermal modelling requires a detailed knowledge of the crustal geometry and its thermophysical parameters (e.g., Čermák et al., 1993; Zeyen et al., 2002; Fernàndez et al., 2004). Deep seismic profiling and regional tomography also provide images of the lithospheric structure based either on the interpretation of absolute wave propagation velocities or the travel time residuals relative to a global reference model (e.g. Lay and Wallace, 1995; Levshin et al., 2001).

Some of the main parameters controlling the final outputs of thermal and seismic models are the elastic parameters (i.e. bulk and shear modulus) and the coefficient of thermal expansion (CTE) assumed for the lithospheric mantle. The former controls wave velocities, and therefore the interpretations regarding the thermal state and composition of the mantle. The latter also affects wave velocities, but more importantly, it determines the density of the materials, and consequently the calculated elevation, gravity, and geoid fields. Although there have been numerous attempts to obtain representative values of the CTE for the whole mantle, there are still ambiguities as to which are the appropriate values for the lithospheric mantle. Proposed average values given by different authors range from as low as $1.6\times10^{-5}\,\mathrm{K}^{-1}$ (Stacey, 1992) to as high as $4.2\times10^{-5}\,\mathrm{K}^{-1}$ (Doin and Fleitout, 1996), and they are commonly used indistinctly for lithospheres of different composition and thermal state. Similarly, P_n wave velocities are also assumed to be homogeneous (with typical values of $\sim$8.0 km s^{-1}) over long distances, while they have been shown to be highly variable, ranging from $\sim$7.6 to 8.6 km s^{-1} for lithospheres of different ages (e.g. Németh and Hajnal, 1998; Levshin et al., 2001). Moreover, geophysical models usually consider a homogeneous lithospheric mantle, with a composition rich in olivine, mechanically strong, and denser than the underlying asthenosphere. This picture is rather simplistic, and it is in disagreement with recent data that indicates that lithospheres of different nature (i.e. oceanic versus continental) and ages have distinct compositional and mechanical properties (e.g. Griffin et al., 1999; Peccerillo and Panza, 1999; O'Reilly et al., 2001; Niu et al., 2003; Afonso and Ranalli, 2004; and references therein). Hence, it is of interest to determine representative values of the elastic properties and CTE for different lithospheres that permit a more accurate modelling.

In this paper, we explore systematically the heterogeneity of the lithospheric mantle and determine representative values of CTE and elastic parameters for lithospheres of different nature and ages. The first two sections of the paper are devoted to introduce the models used to calculate both elastic parameters and CTE of rocks. Subsequently, we discuss the composition and lateral heterogeneities of the lithospheric mantle, and the applicability of our methodology to estimate P-wave velocities and CTE in this region.

In contrast to the majority of previous studies, where values are calculated from inversion techniques or experimental data on olivine only (e.g. Parsons and Sclater, 1977; Stein and Stein, 1992; Doin and Fleitout, 1996; Aizawa et al., 2001), our approach will rest exclusively on mineral physics of composites. This approach has several advantages over the previous analyses due to: (a) inversion techniques imply an assumed physical model that fully describes the evolution of the system (e.g. plate model, half-space cooling model), which does not exist for continental lithosphere; (b) inversion models give "homogenized" values for the materials, and therefore cannot provide relationships between composition and physical parameters; (c) only mineralogical data give information about the temperature and pressure dependence of the parameters; (d) compositional heterogeneities prevent the use of experimental data on olivine only; and (e) this methodology is the only one that provides an independent approach to test previous estimations.

The elastic properties of mantle rocks, based on the properties of its constituents only (i.e. minerals), are calculated by means of the shear-lag model (Cox, 1952), which is here improved and expanded for three-phase rocks. It is shown that our model gives excellent predictions of Young's modulus for two-phase composites, and good estimates of wave velocities for three-phase rocks. This model is preferred over other models (Reuss–Voigt–Hill; Hashin-Shtrikman, etc.) because it is the only one that can be used to calculate stress-distribution processes within the material and between the phases, providing a promising approach for future rheological considerations. The CTE is calculated using systematics in the pressure–temperature dependence of volume for the main constituents of the uppermost mantle. The usual rule of mixtures is applied to estimate the CTE of the composite, since this method gives the best predictions at temperatures pertaining the lithosphere. The obtained results and their implications in terms of lithospheric modelling are discussed for lithospheres of different age and nature. We compare our results for oceanic lithosphere with those obtained from inversion techniques, which should coincide if both approaches are valid. Finally, we discuss the major sources of error in the model and their impact on the final results.

2. Elastic properties

2.1. Two-phase composites

The shear-lag model was originally proposed for describing the effect of stress transfer from the matrix to the embedded discontinuous fibres in fibre-reinforced composites (Cox, 1952). Although the original model only considers the load transfer from the matrix to the fibres by means of shear stresses at the fibre–matrix interface, several modifications have been made to account for the stress transfer across the fibres ends (e.g. Nair and Kim, 1992; Hsueh, 1995; Zhao and Ji, 1997; Starink and Syngellakis, 1999; and references therein). The analytical solutions obtained from the governing equations, and therefore the accuracy of the model, are largely dependent on the imposed boundary conditions at the fibre end. A common approach is to set stress boundary conditions, based on various arbitrary assumptions (e.g. Clyne, 1989; Nair and Kim, 1992). However, as Hsueh (1995) pointed out, this stress is not a predetermined value, and therefore the boundary conditions cannot be chosen unambiguously. Here we adopt a scheme similar to that described in Hsueh (1995), with general boundary conditions based only on well-established mechanical principles. The formulation is, however, modified in order to express the final analytical solutions in a simple closed form and to extend the model from two to three-phase composites.

The unit cell is shown in Fig. 1. It is composed of a uniform cylindrical matrix of length $2L$ and radius R, containing a discontinuous cylindrical fibre with radius r_1 and length $2l$. Fibre and matrix are coaxial, and cylindrical coordinates r, θ, and x apply, where r and θ are the polar coordinates of the projection of a point P in the polar plane, and x is the distance from the polar plane, taken at the mid-point of the unit cell, to the point P. The unit cell is subject to a uniform tensile stress σ_a at its ends, where only the matrix is present. The applied stress is parallel to the fibre axis, and it is assumed that there is no sliding between the matrix and the fibre at the interface $r = r_1$. At this interface, because the Young's moduli of the two phases are different, stresses from the matrix are transferred to the fibre by interfacial shear. In the same way, an axial stress $\sigma_f(x)$, which is considered to be independent of r, is also transferred at the ends of the fibre. The assumption of no sliding between matrix and fibres implies that the interfacial strength is

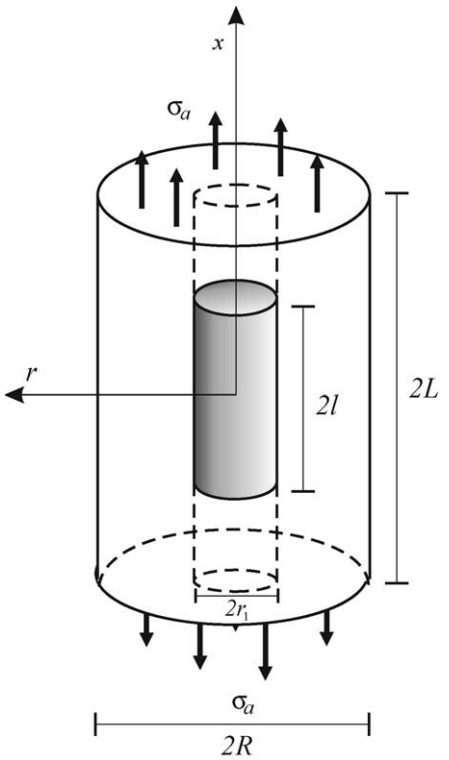

Fig. 1. Schematic drawing of the unit cell and coordinate axes used for analyzing the stress transfer between the matrix and the short fibre (shaded). Dashed cylindrical volumes represent the imaginary fibres added to analyze the stress transfer at the fibre ends.

high enough to resist dissipative mechanisms such as grain boundary sliding, and therefore anelastic effects are negligible. We will show further in this paper that this is a suitable assumption for calculating P-wave velocities at pressures and temperatures pertaining to the lithosphere (see Section 7).

Since the axial and shear stress distribution in and along the fibre are symmetric with respect to the r-axis, the equations describing these stresses can be written as (see Appendix A):

$$\sigma_{\mathrm{f}}(x) = \frac{R^2 E_{\mathrm{f}} \sigma_{\mathrm{a}}}{S} + 2A\cosh(\beta x) \tag{1}$$

$$\tau_{\mathrm{f}}(r_1, x) = -r_1 \beta A \sinh(\beta x) \tag{2}$$

where E_{f} is the Young's modulus of the fibre, and H, S and β are given in Eqs. (A14), (A15) and (A17) of Appendix A.

The coefficient A needs to be determined from boundary conditions. Here we follow an approach similar to that proposed by Hsueh (1995), where two fictitious fibres (made of the matrix material), each with length $L - l$ and width $r = r_1$ are added in the region between the fibre and the ends of the unit cell (dashed in Fig. 1). This approach is the only one which gives analytical solutions for the stress distribution in the matrix region beyond the limit $x = l$.

The far end of the fictitious fibre (i.e. at $x = \pm L$) and the matrix are acted upon by the uniform stress σ_{a}. The fictitious fibre transfers this stress to the bonded ends of the real fibre, but because of the distortion of the stress field in the matrix due to the presence of the strong fibre, the magnitudes of $\sigma_{\mathrm{f}}(l)$ and σ_{a} are neither the same nor a prescribed value, as assumed in some previous work (e.g. Nardone, 1987; Clyne, 1989; Zhao and Ji, 1997; Starink and Syngellakis, 1999). Because of the similar geometry, we can use Eqs. (1) and (2) to describe the stress transfer through and along the fictitious fibre, $\sigma_{\mathrm{ff}}(x)$ and $\tau_{\mathrm{ff}}(r_1,x)$, simply by replacing the Young's modulus of the matrix E_{m} for E_{f} in Eqs. (1) and (2). However, since the stress distribution in the fictitious fibre is not symmetric with respect to the mid-point of the fibre (as it is in the real fibre), Eqs. (1) and (2) can be rewritten as

$$\sigma_{\mathrm{ff}}(x) = \exp(\beta_{\mathrm{f}} x)c_1 + \exp(-\beta_{\mathrm{f}} x)c_2 + \sigma_{\mathrm{a}} \tag{3}$$

$$\tau_{\mathrm{ff}}(r_1, x) = -\tfrac{1}{2} r_1 \beta_{\mathrm{f}} [\exp(\beta_{\mathrm{f}} x)c_1 - \exp(-\beta_{\mathrm{f}} x)c_2] \tag{4}$$

where c_1 and c_2 are two new constants that need to be determined from boundary conditions, and

$$\beta_{\mathrm{f}} = \sqrt{H} \tag{5}$$

The most general boundary conditions that can be applied to the unit cell are (Hsueh, 1995):

$$\sigma_{\mathrm{ff}}(L) = \sigma_{\mathrm{a}}; \quad \sigma_{\mathrm{f}}(l) = \sigma_{\mathrm{ff}}(l);$$
$$\tau_{\mathrm{f}}(r_1, l) = \tau_{\mathrm{ff}}(r_1, l); \quad \tau_{\mathrm{f}}(r_1, 0) = 0 \tag{6}$$

Solving Eqs. (1)–(4) with consideration of boundary conditions (6) yields the following solutions for the constants A, c_1, and c_2

$$A = \frac{\frac{\sigma_{\mathrm{a}}(R^2 - r_1^2)(E_{\mathrm{m}} - E_{\mathrm{f}})}{S}}{\left\langle 2\cosh(\beta l) - \frac{\beta\{2\sinh(\beta l)[\exp(\beta_{\mathrm{f}} l) - \exp(\beta_{\mathrm{f}}(2L - l))]\}}{\beta_{\mathrm{f}}\{\exp(\beta_{\mathrm{f}} l) + \exp[\beta_{\mathrm{f}}(2L - l)]\}} \right\rangle} \tag{7}$$

$$c_1 = 2\frac{\beta A \sinh(\beta l)}{\beta_f\{\exp(\beta_f l) + \exp[\beta_f(2L - l)]\}} \quad (8)$$

$$c_2 = -c_1 \exp(2\beta_f L) \quad (9)$$

Predicted stresses in the fibre and the matrix using Eqs. (1)–(4) are given in Fig. 2. As found previously (e.g. Nair and Kim, 1992; Hull and Clyne, 1996; Zhao and Ji, 1997), the interfacial shear stress reaches a maximum at the fibre ends and a minimum at the mid-point. The axial stress undergoes a significant amplification from the applied stress at the end of the unit cell, σ_a, to the stress $\sigma_f(l)$ acting at the fibre ends. This effect was verified by finite element analysis (Nair and Kim, 1992; Hsueh, 2000), and challenges previous assumptions regarding the stress at the fibre ends (e.g. Nardone, 1987; Zhao and Ji, 1997).

Eqs. (1)–(9) can be used to predict the elastic constants of two-phase composites. The analysis can be done basically in two different ways: (a) by calculating average stresses and strains, or (b) by calculating average displacements. Both schemes give similar results, though the former is somewhat more tedious. The details of the derivation of the equations for these two methods are given in Appendix B. The Young's modulus of the two-phase composite from the shear-lag model is obtained from

$$E_c = L\sigma_a\left\langle \frac{L\sigma_a}{E_m} + \left(\frac{2A\sinh(\beta l)}{\beta} + \frac{lR^2E_f\sigma_a}{S}\right) \times \left(\frac{1}{E_f} - \frac{1}{E_m}\right)\frac{r_1^2}{R^2}\right\rangle^{-1} \quad (10)$$

where S, β, and A are given by Eqs. (A15), (A17) and (7), respectively. The values predicted by Eq. (10) are compared with extensive experimental data and finite element analysis in Fig. 3. Excellent agreement between the published data and the predicted Young's modulus of the composites was obtained in all cases. Also plotted in Fig. 3 are predictions based on the equations presented by Ji and Wang (1999) to fit the experimental data on hot-pressed olivine–enstatite composites, and those obtained from the Reuss–Voigt–Hill (R–V–H) average method (Hill, 1952). Eq. (10) always provides good predictions, even when other methods fail to do so. Note that the apparent lesser accuracy of predictions in Fig. 3g in comparison with the rest of the figures is a false impression due to the scale used in this

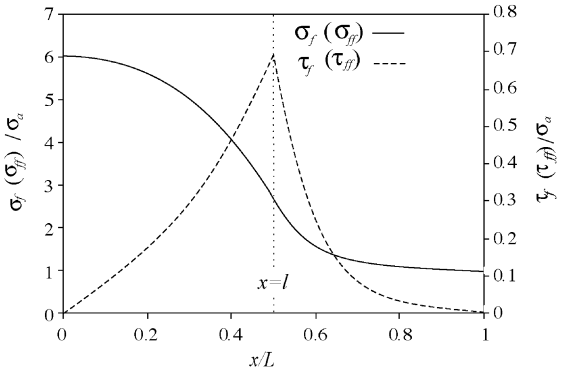

Fig. 2. Normalized axial and shear stresses predicted by Eqs. (1)–(4) for $E_f/E_m = 10$, and $V_f = 0.15$ as a function of the normalized axial distance from fibre midpoint. σ_f and τ_f are the axial and shear stresses in the real fibre and at its interface, respectively. σ_{ff} and τ_{ff} are the axial and shear stresses in the matrix region (i.e. fictitious fibre).

figure and the small difference between the Young's moduli of the phases ($E_f/E_m = 1.08$). The mean absolute error is 1%, which is about the same assigned to velocity measurements from which the moduli are derived (S. Ji, pers. commun.). The non-linearity of the experimental results of Ji and Wang (1999) seems to be related to the microstructural evolution of phase connectivity and continuity in the samples (S. Ji, pers. commun.), although unquantifiable porosity effects also might affect the results (Ji and Wang, 1999).

2.2. Three-phase composites

In this section, we derive simple analytical expressions for the elastic properties of three-phase composites based on the shear-lag model discussed in the previous section. The structure of a composite having two minor phases embedded in a matrix is schematised in Fig. 4. A fundamental assumption behind any model for heterogeneous composites is that their heterogeneities can be "homogenized" by choosing a correct representative volume element (RVE). In the case of a rock we can think that if there is a major phase and two minor phases, the matrix of the RVE will be the major phase containing single inclusions (or fibres) with an equivalent volume fraction. The volume fractions are represented as

$$f_i = \frac{V_i}{V_c} \quad (11)$$

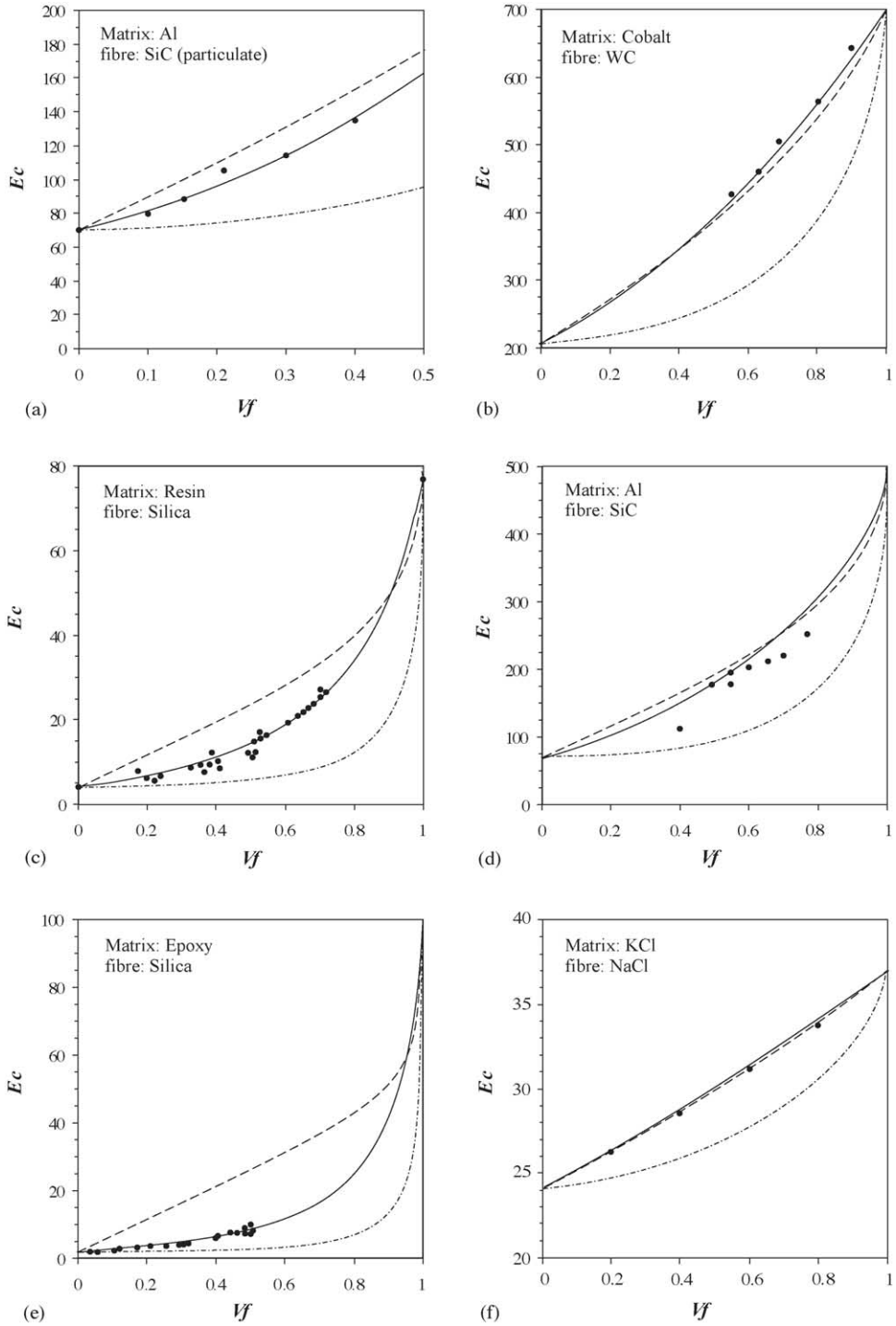

Fig. 3. Comparison of predicted and experimentally determined Young's modulus of various two-phase composites. Experimental data (black dots) from different compilations: (a) Hull and Clyne (1996); (b, c, d, e, i, j) Ravichandran (1994); (f) Watt and O'Connell (1980); (g) Ji and Wang (1999); (h) Hsueh (2000). Full line: results from Eq. (10); dashed line: Voigt–Reuss–Hill average; dashed-dotted line: Ji and Wang (1999).

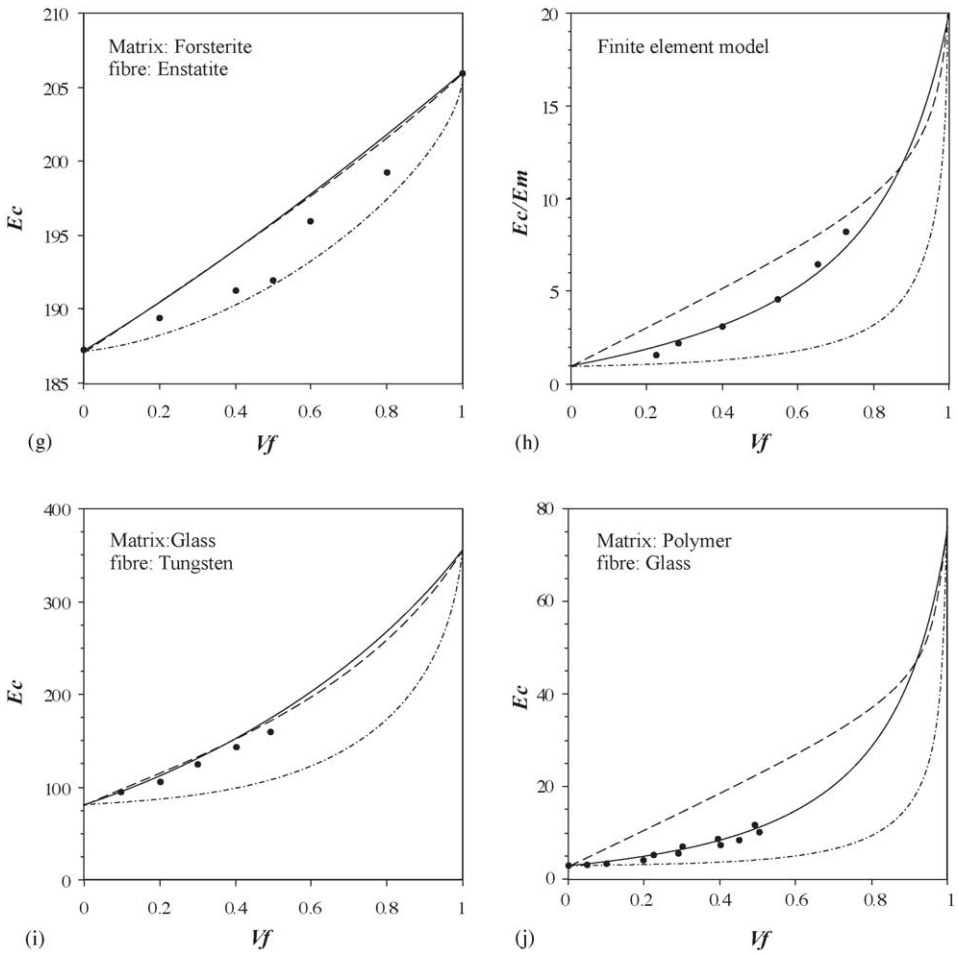

Fig. 3. (*Continued*).

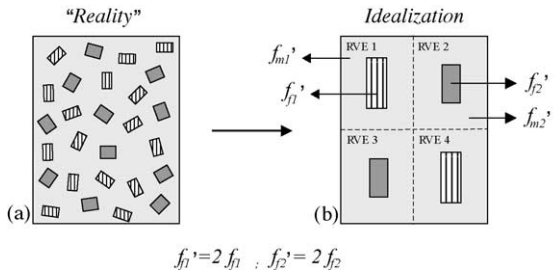

Fig. 4. Scheme of a "real" rock (a) and of the mechanical idealization (b) for analysing the Young's modulus of three-phase composites.

where f_i is the volume fraction of the i-phase and V_i and V_c are the volumes of the i-phase and of the composite, respectively. Hence, the following relation holds for a three-phase composite:

$$V_{f1} + V_{f2} + V_m = V_c \tag{12}$$

The real structure of the rock (Fig. 4a) is idealized in Fig. 4b as a combination of four RVE, each containing one fibre that represents the sum of the volumes of the crystals of one single phase divided by two. The fibres account for the integrated mechanical interaction of many single crystals. The choice of this particular configuration of four RVE is justified since it is suitable to assume that, on average, the rock will contain grains

that interact mechanically as elements in series and in parallel at the same time. Therefore, we must take into account these two mechanisms in describing the final Young's modulus of the composite. Referring to Fig. 4, the total volume V'_c in RVE 1 is

$$V'_c = \tfrac{1}{4}(V_{f1} + V_{f2} + V_m) \tag{13}$$

and also

$$V'_c = V'_{f1} + V'_{m1} \tag{14}$$

where V'_{m1} and V'_{f1} are the new matrix and fibre volumes, respectively. The latter is

$$V'_{f1} = \tfrac{1}{2}V_{f1} \tag{15}$$

Substituting Eq. (15) into (13) and (14) we have

$$V'_{m1} = -\tfrac{1}{4}V_{f1} + \tfrac{1}{4}V_{f2} + \tfrac{1}{4}V_m \tag{16}$$

from which we obtain the volume fraction of the matrix in RVE 1.

$$f'_{m1} = \frac{V'_{m1}}{\frac{1}{4}V_c} = f_{f2} + f_m - f_{f1} \tag{17}$$

In the same way, the volume fraction of the fibre in RVE 1 is

$$f'_{f1} = \frac{\frac{1}{2}V_{f1}}{\frac{1}{4}V_c} = \frac{2V_{f1}}{V_c} = 2f_{f1} \tag{18}$$

The new volume fractions for the fibre f'_{f2} and the matrix f'_{m2} in the RVE 2 can be calculated following the same procedure to give

$$f'_{m2} = f_{f1} + f_m - f_{f2} \tag{19}$$

$$f'_{f2} = 2f_{f2} \tag{20}$$

With these expressions for the volume fractions of the RVE, it is possible to calculate Young's modulus for each RVE by using Eq. (10). Only two moduli are needed, since the modulus of the RVE 1, E_{c_1}, is equal to that of the RVE 4, and the same situation applies for RVE 2 and RVE 3, both of them having modulus E_{c_2}.

In order to obtain the Young's modulus of the three-phase composite, RVE acting in series (i.e. RVE 1 with RVE 3, and RVE 2 with RVE 4) are considered to undergo isostress, while the two RVE acting in parallel (i.e. RVE 1 + 3 with RVE 2 + 4) are assumed to undergo isostrain load conditions. Ravichandran (1994) followed a somewhat similar approach in the unit cell model for two-phase composites. The Young's modulus E_{CA} resulting from the combination of RVE 1 and 3 is therefore

$$E_{CA} = \frac{E_{c_1}E_{c_2}}{E_{c_1}f_2 + E_{c_2}f_1} \tag{21}$$

where E_{c_1} and E_{c_2} are the Young's moduli of the unit cells containing fibres of the phases 1 and 2 (given by Eq. (10)), respectively, and f_1 and f_2 are the volume fractions of each RVE, considered to be the same and equal to 1/2. By means of Eq. (21) and the isostrain condition, the final modulus of the three-phase composite E_{CT} can be expressed as

$$E_{CT} = \frac{E_{c_1}E_{c_2}}{E_{c_1}f_2 + E_{c_2}f_1}(f_1 + f_2) + \frac{E_{c_1}E_{c_2}}{E_{c_1}f_2 + E_{c_2}f_1}(f_1 + f_2) \tag{22}$$

which, since $(f_1 + f_2)$ is now equal to 1/2, it can be rewritten as

$$E_{CT} = \frac{2E_{c_1}E_{c_2}}{E_{c_1} + E_{c_2}} \tag{23}$$

In order to check the validity of our model for predicting elastic constants of rocks composed of three phases, we compare our results with experimental data on different rocks. In doing this, it is important to select only data on three-phase rocks for which the modal composition is known. Also, the change in elastic moduli with temperature and pressure needs to be considered for each mineral before using Eqs. (10) and (23). Table 1 lists modal compositions and Young's moduli used in the calculations. There are, however, three limitations that affect the quality of the comparisons: (a) published elastic moduli are not obtained in uniaxial or triaxial tests, as it would be preferred, but they are estimated from velocity measurements assuming isotropy and homogeneity for both monomineralic aggregates and polymineralic composites; (b) because of the boundary conditions applied to the model, its predictions are expected to give upper bound values; and (c) this kind of data is limited in the literature.

We assume, therefore, that Young's modulus E, shear modulus G, Poisson's ratio ν, bulk modulus K, and P-wave velocities V_p, can be calculated from elasticity relationships for isotropic and homogeneous materials (cf. Lay and Wallace, 1995). The Poisson's ratio

Table 1
Modal compositions (vol.%) and Young's moduli E used in Eqs. (10) and (23) for the four tested rocks

Rock	Composition	E (GPa)[a]
Peridotite[b] S1-S3-S32 (at 0.6 GPa)	Ol (73%)	197.2
	Opx (21%)	187.2
	Cpx (6%)	167
Harzburgite[b] BD1675 (at 1 GPa)	Ol (60%)	201.22
	Opx (24%)	190
	Serp (16%)	43.2[c]
Charnockite[b] A2 (at 0.4 GPa)	Fsp (64%)	69.9
	Qz (30%)	95.56
	Opx (6%)	186
Eclogite[b] XG 98-15 (at 0.6 GPa)	Cpx (50%)	167
	Grt (42%)	243
	Mica (8%)	90

Ol: olivine; Opx: orthopyroxene; Serp: serpentine; Fsp: feldspars; Qz: quartz; Cpx: clinopyroxene; Grt: garnet.
[a] Calculated from data in Bass (1995).
[b] From database in Ji et al. (2002).
[c] Calculated from a rock sample with 98% chrysotile and lizardite (Christensen, 1979).

of the composite ν_c is calculated with the following formula:

$$\nu_c = f_{f1}\nu_{f1} + f_{f2}\nu_{f2} + f_m\nu_m \quad (24)$$

where ν_{f1}, ν_{f2}, and ν_m are the Poisson's ratios of the fibre 1, fibre 2, and matrix, respectively. Although Eq. (24) is strictly an expression for the longitudinal Poisson's ratio (see e.g. Hull and Clyne, 1996), since we are using the fibre configuration as an averaging method, there is no a priori obstacle for not using Eq. (24). Predictions for V_p from Eq. (23) combined with Eq. (10) are compared with available data in Fig. 5. The model provides a good estimate of the measured values, similar to those predicted by the well-known R–V–H average method. The absolute error is found to be $\lesssim$2% in all cases, which lies well within the best predictions associated with other methods (see e.g. Ji et al., 2003).

3. Thermal expansion coefficient

3.1. General considerations

The volumetric coefficient of thermal expansion (CTE) is one of the most important thermophysical parameters in modelling the dynamics of the Earth's interior. It controls the density of the materials, and therefore fundamental processes such as isostasy, magma migration, slab subduction, plume structure, and mantle convection (e.g. Hansen et al., 1993; Ketcham et al., 1995; Suzuki et al., 1998; Schubert et al., 2001; Schmeling et al., 2003). Despite the significance of the CTE in geophysical modelling, there is no consensus regarding the appropriate values for lithospheric mantle materials for both oceanic and continental lithospheres. Currently used values [varying from $(1.6–2.0)\times10^{-5}\,K^{-1}$ (Stacey, 1992; Jing et al., 2002) to $4.2\times10^{-5}\,K^{-1}$ (Doin and Fleitout, 1996)] are generally based only on experimental data on olivine crystals and/or on inversion techniques, and lateral heterogeneities are not taken into account.

A number of models have been proposed to model the CTE of composites, among which the Turner, Kerner, Eshelby, and Garmong models are the most popular (cf. Hahn, 1991). However, besides the fact that they are used only for two-phase composites, these models account for the elastic interactions between phases, and none of them gives good estimates of the CTE when the phases are free to flow in a ductile manner. When this is the case, the simple rule of mixtures provides the best predictions (e.g. Hahn, 1991; Skirl et al., 1998):

$$\alpha_c = \sum_{i=1}^{i=n} \alpha_i V_i \quad (25)$$

where α_c is the CTE of the composite, α_i and V_i are the CTE and the volume fraction of the i-phase, respectively, and n is the number of phases present in the composite. In the upper mantle, the fastest changes in temperature capable of generating elastic thermal stresses are associated with advection of material (e.g. slab subduction, plume rising). However, these processes have lower rates than those at which thermoelastic stresses can be relaxed by rock creep. Therefore, Eq. (25) is expected to give the best approximations of the CTE of the composite.

3.2. Pressure and temperature dependence of CTE

The effect of temperature and pressure on the thermal expansivity of the phases must be taken into

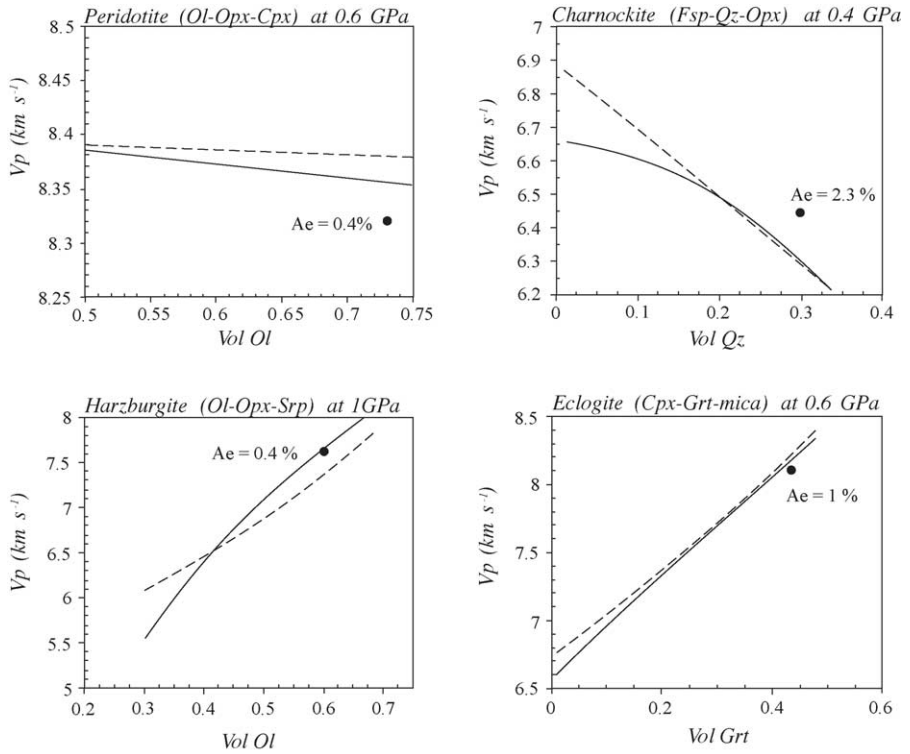

Fig. 5. Comparison of predicted and measured P-wave velocities as a function of the volume fractions of different minerals. In all cases, the volume fraction of the matrix is maintained constant while the volume fraction of the phases are changed continuously (see Table 1). Solid lines are the predictions of the model using Eqs. (10), (23), and (24). Dashed lines are Voigt–Reuss–Hill averages. Black dots represent experimental data. Ae is the absolute error (%), calculated as $(|V_{\text{predicted}} - V_{\text{measured}}|/V_{\text{measured}}) \times 100$. In all the cases, the three main constituents comprise >98% of the sample.

account before using them in Eq. (25). The thermal dependence is usually expressed as a polynomial expansion of the form (Fei, 1995):

$$\alpha(T) = a + bT + cT^{-2} \tag{26}$$

where a, b, and c are coefficients determined experimentally. The density at a given temperature $\rho(T)$ can therefore be calculated as

$$\rho(T) = \rho_0 \left(1 - \int_{T_r}^{T} \alpha(T)\,\mathrm{d}T\right) \tag{27}$$

where ρ_0 is the density at a given reference temperature T_r.

The effect of pressure on the CTE becomes important in thick (i.e. cold) lithospheres. Pressure dependence can be described by the Anderson–Grüneisen parameter δ_T (Chopelas, 2000):

$$\alpha(P, T) = \alpha(T)\left(\frac{\rho(P, T)}{\rho(T)}\right)^{-\delta_T \frac{\rho(T)}{\rho(P,T)}} \tag{28}$$

For pressure ranges within the lithosphere it can be assumed that the term $\rho(T)/\rho(P,T)$ in the exponent is equal to unity without introducing significant errors. We have used a typical average $\delta_T = 5.5$, consistent with theoretical and experimental estimations (e.g. Reynard and Price, 1990; Anderson et al., 1992; Chopelas, 2000). The term within brackets represents the relative change in density with pressure (i.e. compression) along an isotherm and is calculated here using the isothermal third-order logarithmic equation of state (ILEoS) (Poirier and Tarantola, 1998):

Table 2
Parameters used in calculating the pressure and temperature effect on the CTE

Mineral	a (K^{-1})	b	c	d[a]	K_0 (GPa)	K'_0	δ_T
Olivine (Fo 92-93)	2.26×10^{-5}	1.3×10^{-8}	1.33×10^{-3}	−0.427	129.43	3.8	5.5
Olivine (Fo 90)	2.37×10^{-5}	1.26×10^{-8}	1.207×10^{-3}	−0.465	129.61	4.2	5.5
Orthopyroxene (Enstatite)	2.947×10^{-5}	2.694×10^{-9}	−0.5588	–	107.8	5	5.5
Clinopyroxene (Diopside)	3.33×10^{-5}	0.0	0.0	–	114	4.5	5.5
Spinel	2.94×10^{-5}	0.0	0.0	–	207.9	5	5.5
Garnet (Pyrope)	2.311×10^{-5}	5.956×10^{-9}	−0.4538	–	169.4	4	5.5

Data compiled form Fei (1995), Knittle (1995), and Suzuki et al. (1998). K_0 = isothermal bulk modulus; K'_0 = pressure derivative of K_0; δ_T = Anderson–Grüneisen parameter.

[a] This parameter is used only for olivine, whose CTE is calculated with $\alpha(T) = a + bT + cT^{-1} + dT^{-2}$ (Suzuki et al., 1998), instead of using Eq. (26).

$$P = K_0 \frac{\rho(P,T)}{\rho(T)} \ln \frac{\rho(P,T)}{\rho(T)} \times \left\langle 1 + \left(\frac{K'_0 - 2}{2} \right) \ln \frac{\rho(P,T)}{\rho(T)} \right\rangle \quad (29)$$

where K_0 and K'_0 are the isothermal bulk modulus and its pressure derivative, respectively, and $\rho(P,T)$ is the density at the given pressure and temperature. Using mineral parameters listed in Table 2, and substituting Eqs. (26) and (27) into (29), changes in density with pressure can be calculated and used in Eq. (28) to obtain $\alpha(P,T)$. The ILEoS is preferred over the well-known third-order Birch–Murnaghan equation of state for simplicity, since both give identical results over the pressure range pertaining to the lithosphere.

The final distribution with depth of the CTE is the result of the combined effects of temperature and pressure. In the case of silicates, an increase in temperature produces an increase in the value of the CTE. This is shown in Fig. 6 for the case of olivine, orthopyroxene, and garnet. Although the temperature derivative of the CTE is slightly different for these minerals (olivine shows the largest variation), all of them obey this general rule. Also plotted in this figure is the pressure effect (dashed lines) on the CTE, calculated with Eqs. (26)–(29), and assuming a continental Phanerozoic type geotherm (see Section 5). It can be seen that the result of increasing pressure is a reduction in the value of CTE for the three minerals. The pressure effect is particularly important in pyroxenes (see Table 2).

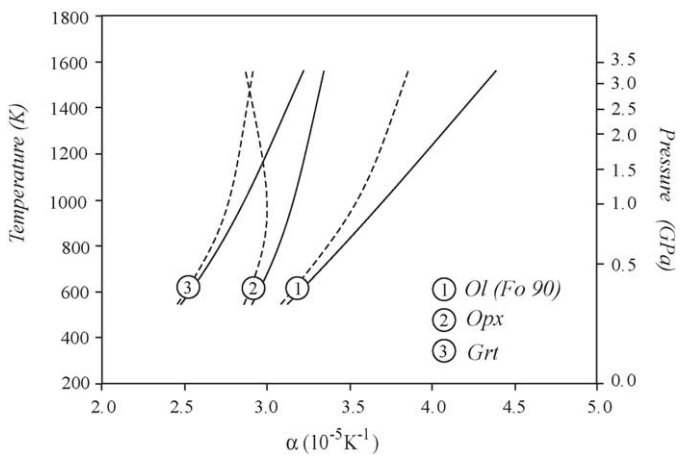

Fig. 6. Variation of the CTE with temperature and pressure for olivine, orthopyroxene, and garnet. Solid lines indicate only the temperature dependence of CTE. Dashed lines include the pressure effect calculated from Eqs. (26)–(29) assuming a continental Phanerozoic type geotherm (see text). Parameters used in calculations are listed in Table 2.

4. Composition and lateral heterogeneities of the lithospheric mantle

There is abundant evidence from xenoliths and geochemical studies on volcanic suites that the lithospheric mantle is highly heterogeneous in composition, both vertically and horizontally (e.g. Wang et al., 1998; Griffin et al., 1999; Peccerillo and Panza, 1999; O'Reilly et al., 2001; Yu et al., 2003; and references therein). However, although these lateral heterogeneities play active roles in geodynamic processes (e.g. Niu et al., 2003), they are often neglected in lithospheric models.

The bulk composition of the lithospheric mantle can be represented as that of a peridotite, but tectonothermal processes can change this average composition considerably from one place to another. Therefore, lithospheres with different tectonothermal histories are expected to have distinctive physical properties and they should be modelled accordingly.

The compositional heterogeneity of peridotitic material in the upper mantle can be modelled by different volume fractions of its three main constituents: olivine, pyroxenes, and an aluminous phase (plagioclase, spinel, or garnet). By definition, a peridotitic rock can vary in composition from almost 100% olivine (dunite) to ∼40% olivine. Rocks with <40% olivine (e.g. pyroxenites, eclogites) are also important components of the lithospheric mantle. Moreover, variations in composition related to age seem to be a well-established fact in the lithospheric mantle, at least for Archean, Proterozoic, and Phanerozoic continental lithospheres (e.g. Hawkesworth et al., 1999; Gaul et al., 2000; Zheng et al., 2001; O'Reilly et al., 2001). As a first approximation, in this paper we distinguish three major lithospheric domains: (a) Archean lithosphere, (b) Phanerozoic continental lithosphere, and (c) oceanic lithosphere.

4.1. Archean lithosphere

Archean lithospheric mantle is characterized by significant amounts of depleted (Fe-poor) harzburgites and lherzolites with high Mg/(Mg + Fe) ratios, strongly subcalcic garnets (low Ca/Al), and low Mg/Si ratios, reflecting the high abundance of orthopyroxene (e.g. O'Reilly et al., 2001; Zheng et al., 2001). Clinopyroxene is subordinate, even in lherzolites, reaching maximum values of ∼3% (Zheng et al., 2001). Olivine ranges from Fo_{92} to Fo_{94} and comprises modal fractions of ∼60% in a typical Archean lithosphere (e.g. Siberia, Kaapvaal, Slave) (Gaul et al., 2000). Orthopyroxene composition is mainly enstatite, which typically reaches modal fractions of ∼32%. These features support the common assumption that Archean lithosphere is the product of high-degree partial melting, which has consumed most of the clinopyroxene during basalt extraction. As a consequence of this continuous Fe removal, the solidus of the mineral assemblage rises while the mean density decreases. Also, since the solubility of water in basaltic melts is approximately three orders of magnitude greater than in mantle minerals (e.g. Hirth and Kohlstedt, 1996), aqueous fluids might have effectively been removed from the Archean lithospheric mantle, leaving a "dry" rheologically strong residue (Afonso and Ranalli, 2004). The combination of relatively low density, low Fe content, "dry" rheology, and low geothermal gradients, makes the Archean lithosphere stable and resistant to mechanisms such as convective thinning, delamination, and reworking.

4.2. Phanerozoic lithosphere

Boyd (1989) and Pearson et al. (1994) were among the first to recognize some fundamental compositional distinctions between Archean and Phanerozoic lithospheric mantles. Phanerozoic continental lithosphere shows the least degree of melt depletion, with high Ca and Al, reaching values close to that of the asthenosphere (O'Reilly et al., 2001). Re-enrichment processes through a number of metasomatic episodes are commonly evidenced in mantle-derived xenoliths, although the extent to which these processes vary the physical properties of the mantle is still unclear (Gaul et al., 2000). Modal clinopyroxene and garnet reach their highest average values, close to 20 and 10%, respectively, although relative abundances can change from one place to another. The Fo content in olivine decreases to $Fo_{90} - Fo_{91.5}$, particularly at shallow lithospheric levels (Gaul et al., 2000; O'Reilly et al., 2001). The less depleted, hotter, and fluid-rich Phanerozoic lithospheric mantle is more likely to be affected by tectonic processes, and it might not contribute significantly to the total strength of the lithosphere (Afonso and Ranalli, 2004).

Table 3
Modal compositions (vol.%) of Archean continental, Phanerozoic continental, and oceanic lithospheres

Lithosphere	Olivine	Orthopyroxene	Clinopyroxene	Garnet	Spinel
Archean	60 (Fo 93-92)	32	3	5	
Phanerozoic	60 (Fo 90)	17	15	8	
Oceanic (<2 GPa)	73.5	21	5		0.5
Oceanic (>2 GPa)	74	19.4	5	1.6	

Estimates are based on several works cited in Section 4.

4.3. Oceanic lithosphere

Typical samples of oceanic lithosphere from which modal compositions can be estimated include abyssal peridotites, harzburgite tectonites, and some Alpine peridotites. Clinopyroxene-free harzburgites and dunites are always subordinate. Abyssal peridotites are the most important for an understanding of the composition of the oceanic lithospheric mantle, since they are thought to represent the residues of mid-ocean ridge basalt (MORB) generation. They show a coarse-grained texture, with grain diameters ranging from 0.1 to 1 cm, and a clear positive correlation between Mg and modal olivine content, reflecting their residual nature (Boyd, 1989). During MORB extraction, infertile abyssal-type peridotites are added to the oceanic plate, forming a shallow layer that will thicken subsequently by thermal accretion. Although the depth at which MORB are generated, as well as the importance of successive modifying processes, are still under debate (e.g. Niu et al., 1997; Baker and Beckett, 1999; Presnall et al., 2002), we follow here the commonly accepted idea that the mean modal composition of abyssal peridotites represent a good estimate for the oceanic lithospheric mantle.

A number of databases containing modal analysis of abyssal peridotites can be found in the literature (see e.g. Dick et al., 1984; Niu et al., 1997; Baker and Beckett, 1999; and references therein). They yield typical modal abundances of 65–84% for olivine, 14–26% for orthopyroxene, and 1–11% for clinopyroxene. Plagioclase is absent, and spinel content is generally less than 0.6%. This range of modal compositions is classically explained in terms of different degrees of partial melting in the source region (Dick et al., 1984), and their averages can be taken as representative of the large-scale oceanic lithospheric mantle composition. The typical average modal compositions for the three domains are listed in Table 3.

5. Geotherms, pressure gradient, and phase change effects

In addition to the influence of compositional variability discussed in the previous section, other factors controlling the physical properties of mineral assemblages are pressure, temperature, and phase changes within the lithosphere. The temperature and pressure effects on mineral properties were already discussed in previous sections. However, in order to give accurate values of CTE and P-wave velocity for the three different lithospheric domains, we need to choose representative pressure and temperature gradients for each domain. The thermal effect is incorporated by solving the steady state, 1D heat conduction equation with radiogenic heat production for a three-layer lithospheric model (i.e. upper crust, lower crust, lithospheric mantle), with type rock parameters and analytical solutions taken from Afonso and Ranalli (2004). The resultant geotherms are shown in Fig. 7. The lithospheric ther-

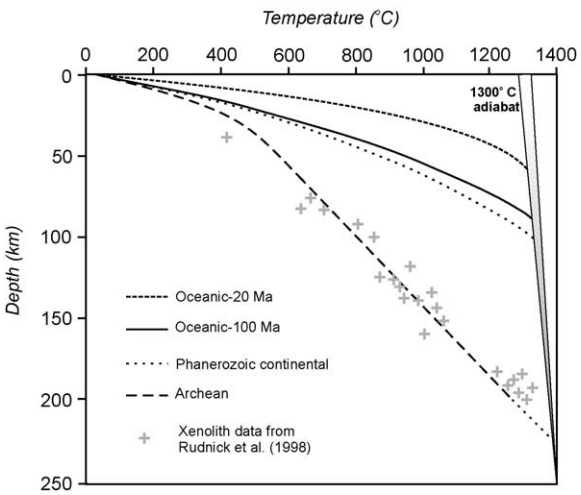

Fig. 7. Type geotherms for the three lithospheric domains considered in this work (modified from Afonso and Ranalli (2004)).

mal thickness is defined for each domain as the depth at which the respective geotherm reaches the 1300 °C mantle adiabat. For comparison, xenolith data from the Siberian, South African, and Tanzanian cratons (Rudnick et al., 1998), are also included. The pressure effect is only important in thick plates, and in the case of the CTE it is simply calculated by assuming an appropriate average density $\overline{\rho}$ for each domain, and using the formula $P_l = \overline{\rho} g z$. Strictly, the lithostatic pressure is a function of temperature, and pressure itself through the CTE, since P_l depends on density (refer to Eqs. (27)–(29)), and independent solutions cannot be obtained simultaneously for $\rho(P,T)$, $P_l\{\alpha(P,T),T\}$, and $\alpha(P,T)$. In this work we adopt the simplification of estimating $\overline{\rho}$ based on temperature only (Eq. (27)). This is justified for typical lithospheric thicknesses, where the ratio $\rho(P,T)/\rho(T)$ is always lower than ∼1.05. Consequently, the lithostatic pressure can be estimated and used in Eq. (29). Since we are considering general end-member domains, detailed crustal structures are not necessary. We take $\overline{\rho}$ in the first 30 km in continental lithosphere to be constant and equal to 2780 kg m^{-3}. In oceanic lithosphere, a constant value of $\overline{\rho} = 2900$ kg m^{-3} was assumed for the first 8 km. The mantle density decreases downwards with increasing temperature following Eq. (27), where ρ_0 is the density of the composite at $T_r = 300$ K, calculated from Eq. (25), replacing α with density. Note that if crustal thickness is modified, parameters will change in response to the pressure variation associated with the change in density. However, pressure effects at Moho levels are relatively unimportant and do not affect significantly the value of the parameters.

Above pressures of ∼2 GPa, a phase transition occurs from spinel lherzolite to garnet lherzolite (e.g. Klemme and O'Neill, 2000), changing the relative volume fractions of the phases. This transition in the system MgO–Al_2O_3–SiO_2 (MAS) can in essence be written as

$$2Mg_2Si_2O_6\,(opx) + MgAl_2O_4\,(spinel) = Mg_2SiO_4\,(olivine) + Mg_3Al_2Si_3O_{12}\,(garnet) \quad (30)$$

from which (taking into account the change in molar volume with pressure and temperature) the new modal composition can be roughly estimated. For example, at 2 GPa and 1300 K, molar volumes of olivine, orthopyroxene, and spinel can be calculated with Eqs. (26)–(29), giving values of ∼45.4, 64.6, and 40.8 cm^3, respectively. Therefore, following the stoichiometry of Eq. (30), an original sample with 0.5 vol.% spinel will be reduced (i.e. after all the spinel is consumed) in orthopyroxene by an amount of ∼1.58%, and enriched in olivine by ∼0.55%.

6. Modelling results

Predicted values of CTE and P-wave velocity were calculated for the three main lithospheric domains defined above. In oceanic lithosphere, two different cases were considered: a "young" lithospheric section of age $\lesssim$20 Ma, and an "old" section of age ∼100 Ma. When four-phase rocks are analyzed, the elastic properties of ortho- and clinopyroxenes are averaged into a single phase taking into consideration their respective volume fractions. In this way, the final elastic modulus M is represented as $M = f_{ortho}M_{ortho} + f_{clino}M_{clino}$. Temperature and pressure effects were calculated using the values in Tables 2 and 4. Results are shown in Figs. 8 and 9 as function of temperature and pressure (i.e. depth). The depth displayed in these figures can be converted to temperature, according to the geotherms in Fig. 7.

6.1. Archean lithosphere

Archean lithosphere shows the simplest pattern in both CTE and seismic velocities. Cold geotherms in these regions preclude a significant increase in the CTE, and are associated with thick lithospheres, which increase the relative importance of the pressure effect on minerals. This is illustrated in Fig. 8a, where at pressures $\gtrsim$1.5 GPa, the pressure effect prevails over the effect of temperature, making the CTE decrease systematically down to depths of ∼200 km. The relatively high content in orthopyroxene (see Table 3) in Archean lithospheres favours this situation because of the strong pressure effect in this mineral (see Fig. 6).

For modelling purposes, the opposite effects of temperature and pressure allow to choose an average value for the whole lithosphere, since the variation with depth is relatively unimportant. Values between (3.04 and 3.11) × 10^{-5} K^{-1} are acceptable. However, changing the geotherm in particular cases can alter

Table 4
Elastic moduli and P–T derivatives of minerals used in calculating wave velocities

Mineral	K_s (GPa)	G (GPa)	$\partial K_s/\partial P$	$\partial K_s/\partial T$ (MPa K^{-1})	$\partial G/\partial P$	$\partial G/\partial T$ (MPa K^{-1})
Olivine (Fo 92-93)	129.4	79.1	5.13	−16.9	1.79	−13.8
Olivine (Fo 90)	129.5	77.6	4.56	−18	1.71	−13.6
Orthopyroxene (Enstatite)	107.8	75.7	9.6	−26.8	2.06	−11.9
Clinopyroxene (Diopside)	114	64.9	4.6[a]	−24[b]	2[b]	−11[b]
Spinel	196.7	108.3	5	−15.7	1.7[c]	−9.4
Garnet (Pyrope-rich)	171.2	92.6	4.93	−19.5	1.56	−10.2

Data compiled from Bass (1995). K_s = adiabatic bulk modulus; G = shear modulus.
[a] Assumed to be equal to $\partial K_0/\partial P$, from Knittle (1995).
[b] Assumed values.
[c] From other spinel structured oxides.

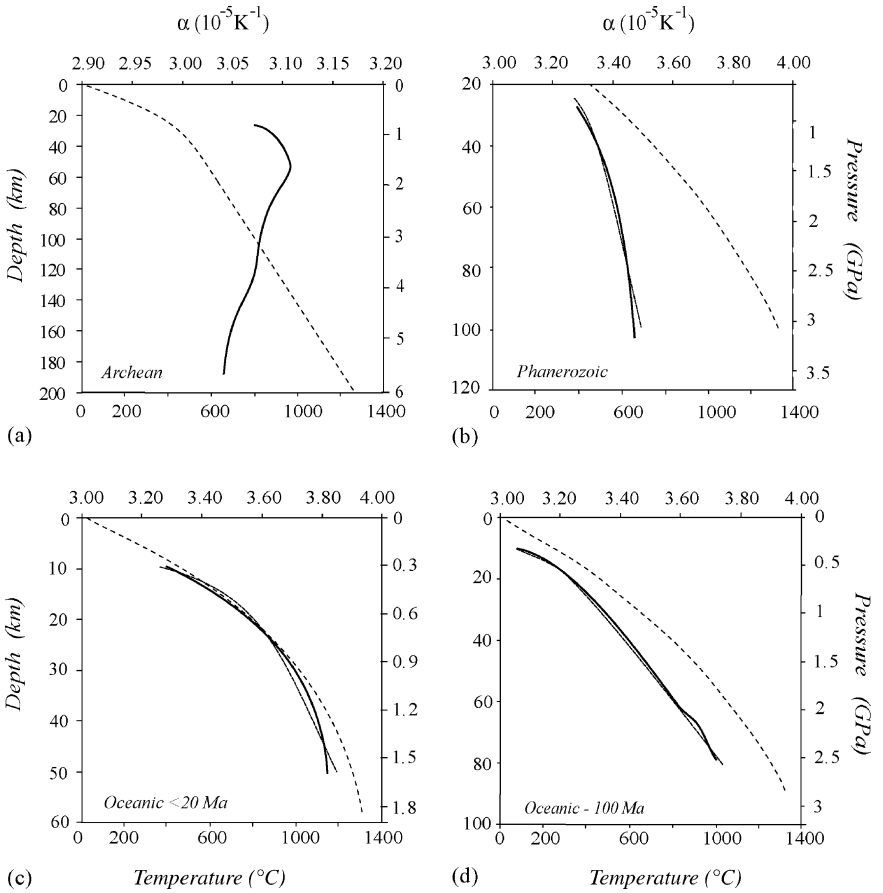

Fig. 8. Variation of the CTE with depth for the three considered lithospheric domains. Solid lines: predictions from the model; dashed-dotted lines: polynomial approximations given in Section 6; dashed lines: type geotherms. Temperature refers only to the geotherms. Note the different horizontal scale used in the Archean (a).

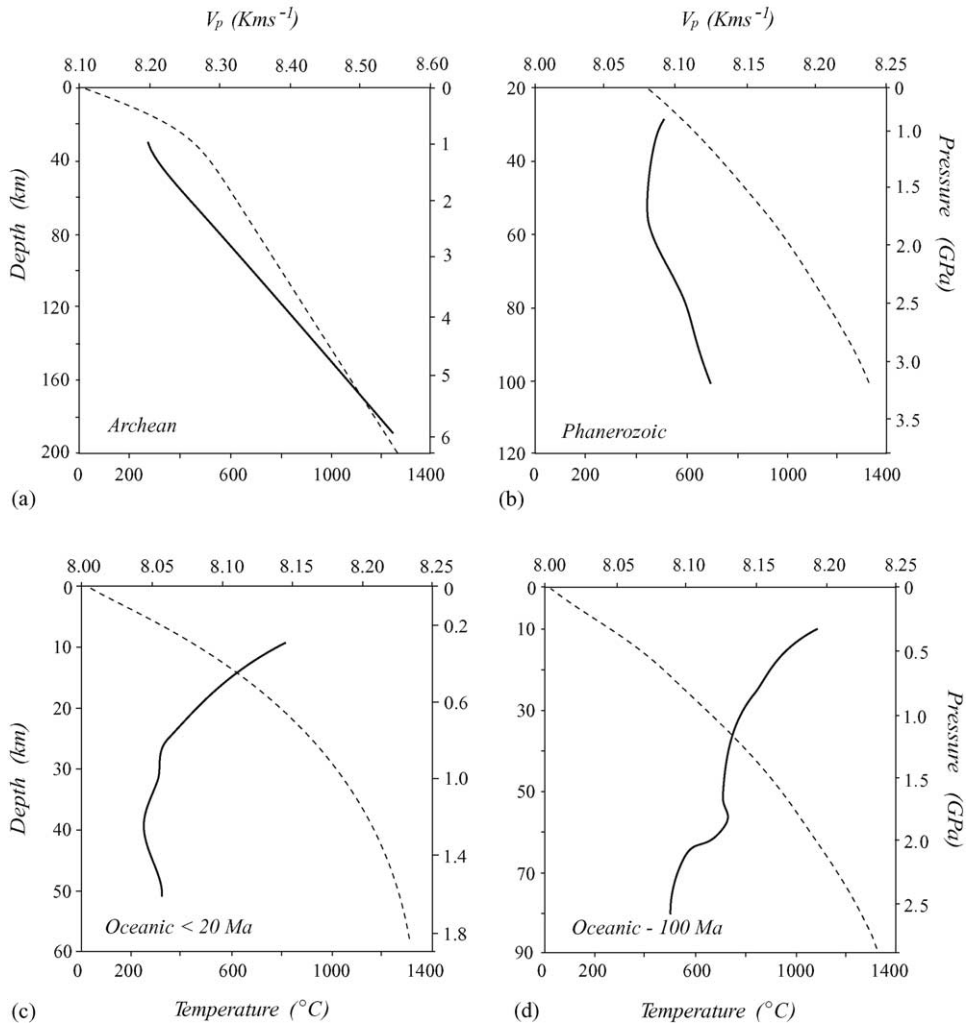

Fig. 9. Variation of the P-wave velocity with depth. Solid lines: predictions from the model; dashed lines: type geotherms. Note the different horizontal scale used in the Archean (a).

these figures. Nevertheless, variations of more than $\pm 0.06 \times 10^{-5}\,\mathrm{K}^{-1}$ are unlikely to occur (see Section 7).

Predicted seismic velocities V_p as a function of temperature and pressure (i.e. depth) are shown in Fig. 9a. Values between 30 and 40 km of depth are in good agreement with estimates of P_n for cratonic areas (e.g. Németh and Hajnal, 1998; Levshin et al., 2001; Grad et al., 2002). Archean lithospheres exhibit a relatively simple pattern of V_p variation. A constant depth-derivative $\partial V_\mathrm{p}/\partial z \sim 2.3 \times 10^{-3}\,\mathrm{s}^{-1}$ is estimated, which yields velocities of $\sim$8.6 km s^{-1} at 200 km of depth, in agreement with estimates from seismic studies (e.g. Balling, 1995; Németh and Hajnal, 1998).

6.2. Phanerozoic continental lithosphere

Predictions for the CTE and P-wave velocities for Phanerozoic continental lithosphere are shown in Figs. 8b and 9b, respectively. Here, the simple patterns revealed for Archean lithosphere disappear. In the case of the CTE, an increase with depth is evident, due to the relatively "hot" geotherm. Since the lithospheric thermal thickness is $\sim$110 km, pressure ef-

fects are moderate and temperature dependence dominates the variation of the CTE. The results indicate a variation from ($\sim$3.3 to 3.5) $\times 10^{-5}\,K^{-1}$ at pressures equivalent to 30 and 100 km, respectively. However, larger variations should be expected with slight changes in the geotherms and/or Moho depths. Neglecting temperature and pressure dependence in the CTE can lead to errors of $\sim$20% in subsidence estimations (e.g. Ketcham et al., 1995) and lithospheric thickness. The predicted variation of the CTE with depth suggests that this parameter can be approximated in numerical models by a simple polynomial expression of the form $\alpha(z) = \alpha_1 + \alpha_2 z - \alpha_3 z^{-2}$, where α_1, α_2, and α_3 are constants of the order of 10^{-5}, 10^{-8}, and 10^{-4}, respectively, whose precise values need to be determined for each particular case. Using the geotherm representative of Phanerozoic lithosphere (see Fig. 7), we find $\alpha(z) = 3.3 \times 10^{-5} + 2 \times 10^{-8} z - 5 \times 10^{-4} z^{-2}$, where z is in km. This expression introduces errors of <1% in the value of the CTE in a depth range of 25–100 km with respect to model predictions. Although a polynomial expression can be useful for modelling purposes, the methodology presented in this work should be used to calculate the pertaining parameters as a function of temperature and pressure whenever possible, since uncertainties in geotherms can result in $\sim$3% error on CTE estimations (see Section 7).

The P-wave velocity variation with depth in Phanerozoic lithosphere shows a complex pattern. A steep decrease is expected in the range 25–40 km, followed by an almost constant value of $\sim$8.08 km s^{-1} between 40 and 60 km, and a systematic increase with a depth-derivative $\partial V_p/\partial z \sim 1.12 \times 10^{-3}\,s^{-1}$ from 60 km downwards. These velocities are in good agreement with the typical P_n values of about 8.0–8.1 km s^{-1} measured in Phanerozoic areas, although the depth-derivative seems to be slightly low. However, the maximum variability is still small (between $\sim$8.08 and 8.13 km s^{-1}, Fig. 9b) and a near constant P-wave velocity is expected in these areas (see Section 7).

6.3. Oceanic lithosphere: $\lesssim$20 and $\sim$100 Ma

Oceanic lithosphere exhibits a variation pattern for the CTE similar to that of Phanerozoic continental lithosphere. However, the amplitude of the variation is larger, due to the higher content in olivine and steeper geotherms. In young plates (age $\lesssim$20 Ma), values of the CTE range non-linearly from (3.25 to 3.82) $\times 10^{-5}\,K^{-1}$ at pressures equivalent to depths of 10 and 50 km, respectively (Fig. 8c). The latter value is the highest CTE found in this work. Again, the non-linear variation pattern precludes the use of a single average value. Using the type geotherm in Fig. 7, a good approximation in a depth range of 8–50 km can be obtained with the polynomial formula $\alpha(z) = 3.5 \times 10^{-5} + 7.2 \times 10^{-8} z - 2.78 \times 10^{-4} z^{-2}$, with z in km. When old lithospheres ($\sim$100 Ma) are considered, and taking into account the phase transformation shown in Eq. (30), values for the CTE are slightly smaller than in young oceanic lithospheres. Predicted values lie in the range of (3.0–3.7) $\times 10^{-5}\,K^{-1}$ at pressures equivalent to depths of 10 and 80 km, respectively, using a type geotherm (Fig. 8d). In this case, the best-fitting function can be expressed as $\alpha(z) = 3.11 \times 10^{-5} + 7.9 \times 10^{-8} z - 1.5 \times 10^{-4} z^{-2}$. Independent estimations of average CTE in oceanic lithosphere have been obtained from inversion techniques. Parsons and Sclater (1977) reported best-fitting values of $(3.28 \pm 1.19) \times 10^{-5}$ and $(3.1 \pm 1.11) \times 10^{-5}\,K^{-1}$ for the North Pacific and North Atlantic, respectively. Stein and Stein (1992) found a slightly smaller value of $(3.1 \pm 0.8) \times 10^{-5}\,K^{-1}$ for the same regions. Doin and Fleitout (1996) obtained values ranging from (3.34 to 4.2) $\times 10^{-5}\,K^{-1}$, with a preferred CTE of $3.85 \times 10^{-5}\,K^{-1}$. Predictions from our model are in very good agreement with the majority of these values. Indeed, our mean CTE for old oceanic lithosphere is $\sim 3.45 \times 10^{-5}\,K^{-1}$. However, our estimates indicate that the values used by Doin and Fleitout (1996) are too large to be used as average values in lithospheric models.

The P-wave velocity variation with depth is plotted in Fig. 9c and d. In the case of young oceanic lithosphere the velocity decreases from $\sim$8.14 to 8.05 km s^{-1} in the first 30 km, from where it follows a nearly constant path downwards. These values are consistent with in situ measurements in young oceanic lithospheres (e.g. Canales et al., 1998), although the rapid variation of the geotherms with distance from the ridge in these regions makes velocities vary considerably (see Section 7). In old lithospheres, a reduction in P-wave velocity with depth is observed. However, the pattern is not simple because of the spinel–garnet

phase transformation at ∼2 GPa. Calculations predict that the velocity starts to increase at about 1.15 GPa in the spinel-lherzolite field. Yet, since elastic properties of garnet are more influenced by temperature (see Table 4) than those of spinel, this effect is blurred, and the overall pattern is gradual reduction in P-wave velocities down to depths of ∼70 km. However, although there is experimental evidence that indicates a narrow transitional zone (e.g. Robinson and Wood, 1998), the depth at which the phase transformation occurs is still unclear (e.g. Robinson and Wood, 1998; Klemme and O'Neill, 2000; Presnall et al., 2002). Consequently, results for this transitional zone are subject to unquantifiable uncertainties.

6.4. V_p anomalies, geoid anomalies, and elevation

Recent numerical algorithms integrate thermal regime and regional observables such as gravity, geoid and elevation in modelling the lithospheric structure (e.g. Zeyen et al., 2002; Fernàndez et al., 2004). The density of the lithospheric mantle and its temperature dependence through the CTE are key parameters linking the equations that describe the lithosphere. The variations of CTE values with composition/age of the lithospheric mantle can have noticeable effects on the calculated elevation and geoid height, and hence on the lithospheric thickness obtained from these integrated lithospheric models. On the other hand, the effect on the gravity anomalies will be almost negligible due to the $1/r^2$ dependence of the gravity field, where r is the distance to the density anomaly. These effects can be quantified in a simple manner by calculating variations in elevation, geoid height, and V_p anomalies relative to a reference model with a typical constant value of $3.5 \times 10^{-5}\,K^{-1}$ for the CTE. In an Archean lithosphere whose mantle extends from a depth of 40 km down to 180–220 km, differences of $\Delta E \sim 270$–348 m and $\Delta N \sim 6$ m relative to the standard model are obtained for topographic elevation and geoid height, respectively. In Phanerozoic lithosphere, variations are much less evident, yielding $\Delta E \lesssim 30$ m and $\Delta N \sim 0.24$ m. For the oceanic domain (water unloaded), differences of $\Delta E \sim 38$ m and $\Delta N \sim 0.15$ m are obtained for the case of a young lithosphere ($\lesssim$20 Ma), and $\Delta E \sim 22$ m and $\Delta N \sim 0.2$ m for an old lithosphere (∼100 Ma). These differences are related to variations in the average lithospheric mantle density as a consequence of the P–T dependence of the CTE. Estimated average density anomalies for the lithospheric mantle are $6.2\,kg\,m^{-3}$ for Archean lithosphere; $1.0\,kg\,m^{-3}$ for Phanerozoic lithosphere; $2.9\,kg\,m^{-3}$ for young oceanic lithosphere; and $0.9\,kg\,m^{-3}$ for old oceanic lithosphere.

Similarly, variations in travel time of P-waves can be estimated by comparing the obtained V_p values (Fig. 9) with those predicted by the PREM model (Dziewonski and Anderson, 1981). For an Archean lithosphere in the depth range between 40 and 220 km, the average calculated P-wave velocities from our model are about 4% higher than those from the PREM model. Such significant residuals are in agreement with global V_p tomography studies, which show deviations of up to +3% in cratonic regions (e.g. Zhou, 1996). Shear wave tomography also displays deviations of up to +6% beneath ancient continental lithospheres (e.g. Ritsema and van Heijst, 2000; Villaseñor et al., 2001), which result in V_p anomalies of ∼4% if we consider that $\mathrm{d}\ln V_s/\mathrm{d}\ln V_p \sim 1.5$ for the first 220 km (Bolton and Masters, 2001). The P-wave velocities obtained from our model are higher than those proposed by O'Reilly et al. (2001) for Archean lithospheres at 100 km depth ($8.18\,km\,s^{-1}$) inferred from the same mineralogical composition used in this paper, but applying a different model for aggregates. However, this value is rather low if we consider that the PREM model proposes a velocity of $8.07\,km\,s^{-1}$ at this depth, which results in an increase of only +1.3%. Actually, deep seismic profiling data show P_n values of 8.25–$8.35\,km\,s^{-1}$ beneath the Baltic Shield and the East European Platform (e.g. Kozlovskaya et al., 2002; Grad et al., 2002) and P-wave velocities of up to 8.5–$8.7\,km\,s^{-1}$ in the range of 125–200 km depth beneath the Fennoscandian Shield (Ansorge et al., 1992). Differences between the predictions of our model and the PREM model are drastically reduced to ±0.3% for Phanerozoic and oceanic lithospheres.

7. Discussion

In this section, we evaluate possible error margins affecting our results as a consequence of seismic attenuation and uncertainties in experimental data and temperature.

7.1. Attenuation effects

The methodology for calculating the elastic properties of composites introduced in Section 2 relies on the assumption that both the fibre ends and the interface along the fibre length are perfectly bonded to the matrix, and therefore the system is considered an elastic medium (see also Appendix A). Models that include debonding and "weak" interfaces have been developed based on the shear-lag model, as well as on other models (e.g. Yoda et al., 1978; Starink and Syngellakis, 1999; Li et al., 1999). They indicate that the average properties of the composite are noticeably dependent on both the physical properties of the interface and the magnitude and frequency of the applied stress. However, when the properties of the interface are not markedly different from those of the phases, and when the magnitude and frequency of the applied stress are relatively small and high, respectively, the effect of debonding is unimportant (Hull and Clyne, 1996; Starink and Syngellakis, 1999). Applied to seismic wave propagation, the assumption of no sliding between phases implies that anelastic effects such as grain boundary sliding are neglected in our approach. In the present context, we request the model to be valid at relevant seismic frequencies ($0.01 < f < 1$ Hz) and at pressure and temperature ranges adequate for the lithospheric mantle, specifically between ~0.5 and 6 GPa, and 200 and 1300 °C, respectively. In this section, we show that physical attenuation (represented in terms of the specific quality factor Q) due to anelastic effects is not a significant factor when calculating P-wave velocities in the lithospheric mantle.

Many studies on the attenuation of seismic waves due to anelasticity have been carried out in the last 30 years (e.g. Kanamori and Anderson, 1977; Minster and Anderson, 1981; Karato, 1993; Gribb and Cooper, 1998; Jackson et al., 2002; and references therein). In summary, the most relevant conclusions concerning the lithospheric mantle drawn from these studies are: (a) at seismic frequencies $0.01 < f < 10$ Hz and temperatures <1000 °C, mantle assemblages are essentially elastic; (b) losses in shear are much more important than in compression (i.e. $Q_K \gg Q_G$); (c) Q is weakly dependent on frequency in the wide range of $0.001 < f < 1$ Hz; and (d) under the reasonable assumption of $Q_K \sim 0$, then $Q_p = (9/4)Q_s$. All of the above indicate that our calculations of P-wave velocities ought to be correct up to temperatures of ~1000 °C, which encloses much of the thermal lithosphere, and that between 1000 and 1300 °C they are much less affected by anelasticity than S-wave velocities. When Q is considered to be slightly frequency dependent, phase velocity of P-waves is related to Q_p by (Minster and Anderson, 1981; Karato, 1993):

$$V_p(T_o, T) = V_{p_o}(T)\left[1 - \left(\frac{1}{2}\right)\cot\left(\frac{\pi\alpha}{2}\right) Q_p^{-1}(T_o, T)\right] \tag{31}$$

where V_{p_o} is the unrelaxed high frequency wave velocity at a given temperature, T_o the oscillation period, and α a constant with values between 0.2 and 0.3. In the range of $1000 < T < 1300$ °C, the Q_s^{-1} for olivine can be adequately represented by

$$Q_s^{-1} = A\left[T_o d^{-1} \exp\left(-\frac{E}{RT}\right)\right]^{\alpha} \tag{32}$$

where d is the grain size, $A = 750\ \mathrm{s}^{-\alpha}\ \mu\mathrm{m}^{\alpha}$, $\alpha = 0.26$, $E = 424\ \mathrm{kJ\,mol}^{-1}$, and R the universal gas constant (Jackson et al., 2002). Substituting Eq. (32) into Eq. (31), and using the relation in (d), we finally obtain for P-waves:

$$V_p(T_o, T) = V_{p_o}(T)\left\{\left[1 - \left(\frac{2}{9}\right)\cot\left(\frac{\pi\alpha}{2}\right) A \left[T_o d^{-1}\exp\left(-\frac{E}{RT}\right)^{\alpha}\right]\right]\right\} \tag{33}$$

Eq. (33) can be used to estimate anelastic effects on P-waves in the temperature range $1000 < T < 1300$ °C. Fig. 10 shows the absolute error in velocity calculations for various representative values of oscillation periods T_o (1 − 100 s). It is clear that for common values of attenuation and seismic frequencies the majority of the data lies well below the value of 0.6%. Only for extreme values of Q_p and frequencies of ~100 and ~0.001 Hz, respectively, Eq. (33) predicts maximum absolute errors of ~1% for P-wave velocities calculated without considering anelasticity. Furthermore, these figures are considered to be upper limits due to the influence of pressure on Q_p, which tends to reduce physical attenuation (e.g. Jackson et al., 2002).

Hence, it is concluded that anelastic effects are not a decisive factor controlling the quality of the results for P-wave velocities in the lithospheric mantle as predicted by our model. It should be emphasized, however, that this conclusion applies only to the lithospheric

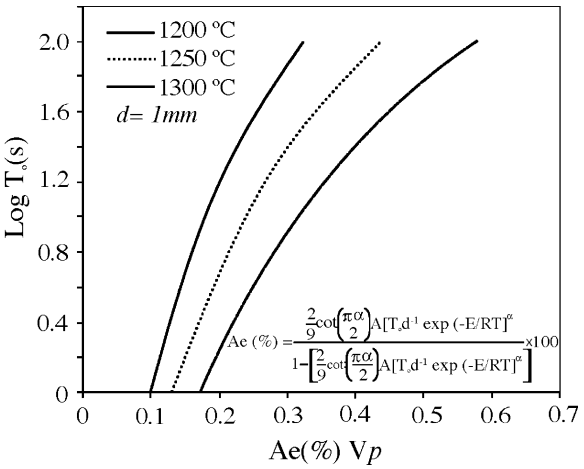

Fig. 10. Absolute errors (Ae) in P-wave velocity calculations as a function of period T_o in the temperature range $1200 < T < 1300\,^{\circ}C$. The error is a measure of the departure of P-wave velocities from elastic behaviour due to anelasticity effects (seismic attenuation) above temperatures of ∼1000 °C. For representative values of T_o (1–100 s), the absolute error is always well below 0.6%, which represent maximum deviations of $+0.05\,km\,s^{-1}$.

mantle (i.e. uppermost upper mantle), and it should not be generalized to the whole upper mantle. Seismic attenuation is a strong non-linear function of temperature, and can be a significant factor at sublithospheric temperatures (e.g. Karato, 1993).

7.2. Uncertainties in experimental mineral data and temperature

Any attempt to estimate the bulk properties of a multiphase aggregate as a function of the individual properties of its constituents is subjected to significant, and often unquantifiable, uncertainties (e.g. Everett and Arsenault, 1991; Hull and Clyne, 1996). The most important factors controlling the estimations of CTE and P-wave velocities for the lithospheric mantle in the present work can essentially be grouped in two different categories: *intrinsic* (i.e. associated with the model and its assumptions) and *extrinsic* (i.e. related to the input data). Intrinsic effects are mainly due to the averaging technique used in estimating both elastic parameters and CTE. Since it is virtually impossible to obtain analytical solutions that include all possible interactions, heterogeneities, and spatial distribution of each phase and of the aggregate, many simplifications have to be made. However, applying well-established physical concepts and suitable combinations of them, the bulk properties of the composite can be approximately evaluated and compared to experimental data to test the validity of the model (cf. Everett and Arsenault, 1991; Hull and Clyne, 1996; see also Ji et al., 2003 for a discussion on errors). Extrinsic factors are more important in the present context for two major reasons: (a) they control the behaviour of the phases due to temperature and pressure changes, and therefore the final properties of the aggregate; and (b) we do not have control on them, and consequently they cannot be modelled accordingly. Foremost among these factors are the uncertainties in experimental mineral data and in the selected geotherm.

Laboratory measurements of elasticity and volumetric CTE of mantle relevant minerals have been actively investigated and detailed compilations of elastic constants, CTE, and their pressure and temperature derivatives are available in the literature (e.g. Anderson, 1988; Fei, 1995; Bass, 1995; Knittle, 1995; Chopelas, 2000). Although experimental errors in single crystals are thought to be negligible, and the isotropic moduli for the same mineral are reasonably consistent among different sources, their temperature and pressure first and second derivatives still exhibit some discrepancies among different authors (e.g. Bass, 1995; Zha et al., 1998; Fujisawa, 1998). Similarly, values of CTE and its derivatives in the literature vary as much as ∼40 and 10%, respectively, for the same mineral (e.g. Saxena and Shen, 1992; Fei, 1995). Also, for clinopyroxenes and spinels, the effect of temperature on the CTE is unknown (Table 2). This scatter in data is difficult to evaluate objectively, since discrepancies are different for different minerals, and possible combinations are unassessable. However, considering the spectrum of values given for these parameters, a sensitivity analysis indicates that calculations of CTE and P-wave velocities might be affected by experimental uncertainties as much as ±8 and ±0.8%, respectively. Refined estimations of elastic parameters for relevant mantle mineral series of complex composition (e.g. pyroxenes and garnet) at lithospheric conditions (e.g. by computational simulations) are still necessary to reduce uncertainties on theoretical estimations.

Uncertainties in the thermal field of a particular region also affect the final results due to the temperature

dependence of mineral properties. Usually, errors associated with stable Archean lithosphere are less important than in Phanerozoic terranes, where surface heat flow can vary between <50 and >90 mW m^{-2} (Artemieva and Mooney, 2001) and the steady-state condition not always applies. Hence, for a common discrepancy of ∼100 °C in geotherms in deep portions of Archean lithosphere, variations of CTE and P-wave velocities as predicted by our model are unlikely to be more than ±2 and ±0.4%, respectively. In Phanerozoic regions, the range of possible geotherms and associated uncertainties are more important, leading to a greater uncertainty in calculated CTE and P-wave velocities. As an example of the variability on the results due to changes in geotherms, we have plotted in Fig. 11 the variation of CTE and P-wave velocity of an average Phanerozoic peridotite (e.g. O'Reilly et al., 2001; Table 3) for a range of realistic geotherms. The spectrum covered by the two mantle geotherms with gradients ∼17 and 10 °C km^{-1} should not be directly correlated with uncertainties in a particular geotherm; it only indicates realistic bounds for possible Phanerozoic geotherms. It can be seen that in the case of seismic velocities, the variation due to the combined effect of temperature and pressure makes the isovelocity lines to be almost parallel to the geotherms (Fig. 11a). This implies that P-wave velocities should not vary considerably with depth in Phanerozoic lithosphere for a given geotherm, consequently reducing the variability associated with uncertainties in the thermal field. Assuming a rather high uncertainty of ∼±15% for a given geotherm, estimation of P-wave velocities should be within the error margin of ±0.6%. In the case of the CTE, iso-CTE lines have a smaller dT/dP value than isovelocity lines, indicating that the pressure effect is slightly less important (Fig. 11b). Since uncertainties in lithostatic pressure are smaller than in temperature for a given geotherm, this change in the slope of iso-CTE lines assigns a somewhat wider error margin to CTE estimations in comparison with P-wave velocities. Assuming the same previous uncertainty for the geotherm, CTE values can be affected by ∼±3% error, which represents possible CTE variations of $\pm 0.1 \times 10^{-5}$ K^{-1}. Following the same procedure, errors for old oceanic lithosphere (>100 Ma) are found to be in the range of ±0.5 and ±2% for P-wave velocity and CTE, respectively. In the case of young oceanic lithosphere (<20 Ma), uncertainties in the thermal field are the greatest due to hydrothermal circulation in the oceanic crust (see Lowrie, 1997), and therefore results for P-wave velocities and CTE are expected to be subjected to errors >±1.5 and ±3%, respectively.

An additional extrinsic source of error results from the average composition chosen to represent a partic-

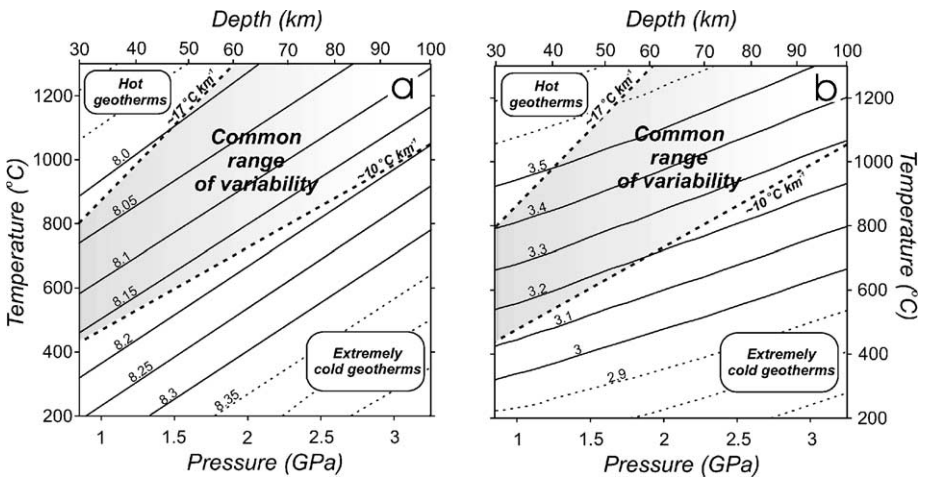

Fig. 11. P-wave velocity and CTE as functions of temperature and pressure for a peridotite with Fo_{90} = 60%, Opx = 17%, Cpx = 15%, and Grt = 8% (Phanerozoic, Table 3). Solid lines are predictions from the model. Attached numbers indicate P-wave velocities in km s^{-1} (a) and CTE values in 10^{-5} K^{-1} (b). Dashed lines represent possible end members of Phanerozoic mantle geotherms (almost linear due to the low radiogenic heat production). Uncertainties of ±15% in any given geotherm within the shaded areas result in variations of ≤±0.05 km s^{-1} (≤±0.6%) and $\sim 0.1 \times 10^{-5}$ K^{-1} (±3%) in P-wave velocities and CTE, respectively.

ular lithospheric mantle. We have used average compositional estimations from xenoliths data thought to be representative of the lithospheric domain (Table 3). Although the oceanic domain seems to be accurately represented by abyssal peridotites (see Section 4), and consistency is found in xenoliths from Archean lithosphere, this might not be true in Phanerozoic domains (e.g. Peccerillo and Panza, 1999; Hawkesworth et al., 1999). However, a formal error analysis is not possible in this case due to the scarcity of detailed information.

The uncertainties discussed above have significant implications on tomography studies. They suggest that errors associated with experimental data and thermal fields can result in velocity anomalies that are comparable to those obtained in seismic tomography (e.g. Zhou, 1996; Vasco et al., 2003). Therefore, even excluding errors induced by the uncertainties on velocity measurements, tomography studies cannot be used to utterly resolve compositional heterogeneities in lithospheric domains with P-wave anomalies $\leq \pm 1.5\%$ (i.e. S-wave anomalies $\leq \pm 3\%$, assuming $\mathrm{d}\ln V_s/\mathrm{d}\ln V_p \sim 1.5$; Bolton and Masters, 2001). Similar results were recently obtained by Artemieva et al. (2004) using global correlation coefficients for attenuation, shear velocity, and thermal structure in the continental upper mantle. It would be particularly useful to integrate the modelling of geoid and gravity anomalies, absolute elevation, and thermal structure, to seismic and xenoliths information to better constrain possible major compositional variations in the lithospheric mantle.

8. Conclusions

We have presented a new approach to calculate elastic properties and CTE of mantle rocks, based on the mineral physics of composites, and considering the spatial heterogeneity of the lithospheric mantle. Analytical expressions are obtained for the elastic properties of two- and three-phase composites on the basis of the shear-lag model, which permits to estimate the stress transfer between phases and seismic velocities of mantle rocks as a function of the volume fractions of its main constituents. Coefficients of thermal expansion of polymineralic rocks are obtained from systematics on the *P–T* dependence of volume of its constituents, and applying an appropriate rule of mixtures. Representative values and related uncertainties have been calculated for three main lithospheric domains. The results can be summarized as follows:

(1) *Archean lithosphere*. This shows the simplest pattern in both CTE and seismic velocities. The effects of temperature and pressure tend to cancel each other, permitting to use a single average value. CTE values between (3.04 and 3.11) $\times 10^{-5}\,\mathrm{K}^{-1}$ are acceptable for numerical modelling. Predicted P-wave velocities of $\sim$8.19 km s^{-1} at 30–40 km are in agreement with P_n estimates in these areas. A constant depth-derivative $\partial V_p/\partial z \sim 2.3 \times 10^{-3}\,\mathrm{s}^{-1}$ is estimated, which yields velocities of $\sim$8.6 km s^{-1} at 200 km depth.

(2) *Phanerozoic continental lithosphere*. No single average value of CTE can be used in modelling these lithospheric sections. Values range non-linearly between (3.25 and 3.47) $\times 10^{-5}\,\mathrm{K}^{-1}$ at pressures equivalent to depths of 25 and 100 km, respectively. A simple polynomial expression is suitable for modelling purposes. The best-fitting function is $\alpha(z) = 3.3 \times 10^{-5} + 2 \times 10^{-8} z - 5 \times 10^{-4} z^{-2}$, where z is depth in km. The P-wave velocity variation with depth exhibits a slight decrease in the range of 25–40 km, followed by almost a constant value of $\sim 8.1 \pm 0.02$ km s^{-1} down to depths of $\sim$100 km. A small depth-derivative $\partial V_p/\partial z \sim 1.12 \times 10^{-3}\,\mathrm{s}^{-1}$ is found from 60 km downwards.

(3) *Oceanic lithosphere*. The amplitude of the variation in the CTE is larger here than in the other domains, due to the higher content of olivine and steeper geotherms in these areas. In young plates ($\lesssim$20 Ma), values of the CTE vary non-linearly from (3.25 to 3.82) $\times 10^{-5}\,\mathrm{K}^{-1}$ at pressures corresponding to depths of 10 and 50 km, respectively. In old lithospheres ($\sim$100 Ma), the CTE is moderately smaller, with predicted values in the range of (3.04–3.7) $\times 10^{-5}\,\mathrm{K}^{-1}$ at 10 and 80 km, respectively. Using type geotherms, good approximation for young and old plates can be obtained with polynomial formulas $\alpha(z) = 3.5 \times 10^{-5} + 7.2 \times 10^{-8} z - 2.78 \times 10^{-4} z^{-2}$ and $\alpha(z) = 3.11 \times 10^{-5} + 7.9 \times 10^{-8} z - 1.5 \times 10^{-4} z^{-2}$, respectively, where z is in km. In the case of young oceanic lithosphere the P-wave velocity decreases from $\sim$8.14 to 8.05 km s^{-1} in

the first 30 km, from where it follows a nearly constant path downwards. For old lithospheres, a systematic reduction in P-wave velocities from ∼8.2 to 8.09 km s^{-1} is predicted at 10 and 80 km, respectively. However, the spinel–garnet phase transformation and uncertainties in the thermal field complicate estimations of P-wave velocities in these regions.

(4) The effects of compositional heterogeneities on topographic elevation and geoid height are particularly noticeable in Archean lithosphere, yielding differences $\Delta E \gtrsim 300$ m and $\Delta N \sim 6$ m, respectively, when compared to a reference model with a CTE standard value of 3.5×10^{-5} K^{-1}. These differences are reduced for Phanerozoic and oceanic lithosphere, which show variations $\Delta E \lesssim 40$ m and $\Delta N \lesssim 0.25$ m for the considered lithospheric thicknesses. Variations in the elastic properties of the lithospheric mantle produce P-wave anomalies of ∼4% in Archean lithosphere, and ≲0.3% for Phanerozoic and old oceanic lithospheres. While the anomalies for Archean lithosphere are certainly significant, those for Phanerozoic and oceanic lithospheres are within the range of experimental and thermal uncertainties, and therefore much less conclusive.

This study shows that significant differences in lithospheric modelling can arise from neglecting mantle compositional heterogeneities, and temperature and pressure effects on important parameters controlling seismic wave velocities, isostasy, and potential fields. Detailed seismic tomography studies and xenolith information should be integrated with gravity and geoid anomalies, elevation, and thermal modelling to explore possible compositional heterogeneities in the lithospheric mantle and to better understand the geodynamic evolution of lithospheric plates.

Acknowledgments

Many colleagues provided valuable comments and discussions on the concepts presented in this paper. Special thanks go to Pedro Corona-Chávez, Jennifer Owen, Brian Cousens, and Keith Bell. We are also indebted to Shaocheng Ji, who kindly provided helpful comments and unpublished data. Assistance by L. Ferres and E. Glinsky is acknowledged. Suggestions by two referees were helpful in the preparation of the final version. This work was supported by Carleton University and OGS (Ontario Graduate Scholarship) Ph.D. scholarships to JCA, an NSERC (Natural Sciences and Engineering Research Council of Canada) discovery grant to GR, and the Spanish research project REN2001-3868-C03-02 to MF.

Appendix A. Stress transfer equations

Force equilibrium in the system (Fig. 1) requires that

$$2\int_0^{r_1} r\sigma_{\mathrm{f}}(x)\,\mathrm{d}r + 2\int_{r_1}^{R} r\sigma_{\mathrm{m}}(x,r)\,\mathrm{d}r = R^2\sigma_{\mathrm{a}} \tag{A1}$$

$$\frac{\mathrm{d}\sigma_{\mathrm{f}}(x)}{\mathrm{d}x} = -\frac{2\tau(r_1,x)}{r_1} \tag{A2}$$

$$r\frac{\partial\sigma_{\mathrm{m}}(x,r)}{\partial x} + r\frac{\partial\tau(x,r)}{\partial r} = -\tau(x,r) \tag{A3}$$

$$2\pi r_1\tau(r_1,x) = 2\pi r\tau(r,x) \tag{A4}$$

where $\tau(r,x)$ and $\sigma_{\mathrm{m}}(r,x)$ are, respectively, the shear and axial stress in the matrix, and $\tau(r_1,x)$ is the shear stress at the matrix–fibre interface.

Hooke's law holds each phase, and therefore we can write

$$\sigma_{\mathrm{f}}(x) = E_{\mathrm{f}}\frac{\mathrm{d}u_{\mathrm{f}}(x)}{\mathrm{d}x} \tag{A5}$$

$$\sigma_{\mathrm{m}}(r,x) = E_{\mathrm{m}}\frac{\partial u_{\mathrm{m}}(r,x)}{\partial x} \tag{A6}$$

$$\frac{\partial u_{\mathrm{m}}(r,x)}{\partial r} = \frac{1}{G_{\mathrm{m}}}\tau(r,x) = 2\varepsilon_{\mathrm{s}} \tag{A7}$$

where E_{f}, E_{m}, G_{m}, $u_{\mathrm{f}}(x)$, $u_{\mathrm{m}}(r,x)$, and ε_{s} are the Young's modulus of the fibre, the Young's modulus of the matrix, the shear modulus of the matrix, the axial displacement of the fibre, the displacement of the matrix, and the shear strain of the matrix, respectively. The axial stress in the fibre is independent of r, and thus $u_{\mathrm{f}}(x)$ and $u_{\mathrm{m}}(r,x)$ must be equal at $r = r_1$ (i.e. no interfacial sliding).

Combining Eqs. (A4) and (A7), and integrating, we obtain (e.g. Hull and Clyne, 1996):

$$\tau(r_1, x) = \frac{(u_m(R, x) - u_m(r_1, x))G_m}{r_1 \ln\left(\frac{R}{r_1}\right)} \tag{A8}$$

where $u_m(R,x)$ and $u_m(r_1,x)$ are the axial displacements of the matrix at $r = R$ and $r = r_1$, respectively, for a given value of x. Combination of Eqs. (A4), (A7), and (A8) gives

$$\frac{\ln\left(\frac{R}{r_1}\right)}{(u_m(R, x) - u_m(r_1, x))} \int_{u_m(r_1,x)}^{u_m(r,x)} du = \int_{r_1}^{r} \frac{dr}{r} \tag{A9}$$

from which $u_m(r,x)$ can be calculated. Assuming an isotropic behaviour for the matrix (i.e. $G_m = E_m/2(1 + \nu_m)$), substitution of $u_m(r,x)$ from Eq. (A9) into (A6) yields

$$\begin{aligned}\sigma_m(r, x) &= E_m \frac{du_m(r_1, x)}{dx} \\ &\quad + \left(E_m \frac{du_m(R, x)}{dx} - E_m \frac{du_m(r_1, x)}{dx}\right) \\ &\quad \times \frac{\ln\left(\frac{r}{r_1}\right)}{\ln\left(\frac{R}{r_1}\right)}\end{aligned} \tag{A10}$$

Recalling that $[du_m(r_1, x)/dx] = [du_f(x)/dx]$, Eq. (A5) permits to rewrite Eq. (A10) as

$$\begin{aligned}\sigma_m(r, x) &= \frac{E_m}{E_f}\sigma_f(x) + \left(E_m \frac{du_m(R, x)}{dx} - \frac{E_m}{E_f}\sigma_f(x)\right) \\ &\quad \times \frac{\ln\left(\frac{r}{r_1}\right)}{\ln\left(\frac{R}{r_1}\right)}\end{aligned} \tag{A11}$$

Using Eq. (A1), we find

$$\begin{aligned}&\frac{du_m(R, x)}{dx} \\ &= \frac{R^2\sigma_a + \left\langle\left(r_1^2 - \frac{R^2 - r_1^2}{2\ln(R/r_1)}\right)\frac{E_m}{E_f} - r_1^2\right\rangle\sigma_f(x)}{E_m\left\langle R^2 - \frac{R^2 - r_1^2}{2\ln(R/r_1)}\right\rangle}\end{aligned} \tag{A12}$$

Finally, differentiating Eq. (A2) with respect to x, and manipulating Eqs. (A4)–(A8) to express $\tau(r_1,x)$ as a function of $\sigma_f(x)$, the following differential equation is obtained:

$$\frac{d^2\sigma_f(x)}{dx^2} = \frac{\sigma_f(x)HS}{E_f R^2} - H\sigma_a \tag{A13}$$

where

$$H = \frac{R^2}{r_1^2(1 + \nu_m)\left\langle R^2 \ln\left(\frac{R}{r_1}\right) - \frac{(R^2 - r_1^2)}{2}\right\rangle} \tag{A14}$$

and

$$S = r_1^2 E_f + (R^2 - r_1^2)E_m \tag{A15}$$

The general solution of Eq. (A13) is of the form $\sigma_f(x) = \sigma_{fH}(x) + \sigma_{fP}(x)$, where $\sigma_{fH}(x)$ is the solution of the homogeneous part and $\sigma_{fP}(x)$ is the solution of the non-homogeneous part (e.g. Kreyszig, 1988). It can be proven that such a solution can be written as

$$\sigma_f(x) = \frac{R^2 E_f \sigma_a}{S} + C_1 \cosh(\beta x) + C_2 \sinh(\beta x) \tag{A16}$$

where

$$\beta = \sqrt{\frac{SH}{R^2 E_f}} \tag{A17}$$

The two constants C_1 and C_2 are determined by applying appropriate boundary conditions. Similarly, from Eqs. (A2) and (A16) we find

$$\tau_f(r_1, x) = -\tfrac{1}{2} r_1 \beta [C_2 \cosh(\beta x) + C_1 \sinh(\beta x)] \tag{A18}$$

Applying the following boundary conditions

$$\begin{aligned}&\sigma_{ff}(L) = \sigma_a; \quad \sigma_f(l) = \sigma_{ff}(l); \\ &\tau_f(r_1, l) = \tau_{ff}(r_1, l); \quad \tau_f(r_1, 0) = 0\end{aligned} \tag{A19}$$

and using Eqs. (A16)–(A18), and (3)–(5), we find the values for the constants C_1 and C_2

$$C_1 = 2\frac{\frac{\sigma_a(R^2 - r_1^2)(E_m - E_f)}{S}}{\left\langle 2\cosh(\beta l) - \frac{\beta\{2\sinh(\beta l)[\exp(\beta_f l) - \exp(\beta_f(2L - l))]\}}{\beta_f\{\exp(\beta_f l) + \exp[\beta_f(2L - l)]\}}\right\rangle} \tag{A20}$$

$$C_2 = 0 \tag{A21}$$

which allows us to rewrite Eqs. (A16) and (A18) in the form of Eqs. (1) and (2) (see also Hsueh, 1995).

Appendix B. Young's modulus of composites

The derivation of the Young's modulus from Eqs. (1)–(9) can be done by two different approaches: (a) using average stresses and strains, or (b) using average displacements.

(a) The fundamental equation describing the modulus of the composite can be written as (e.g. Nair and Kim, 1992):

$$E_c = \frac{(1-f_f)\bar{\sigma}_m + f_f\bar{\sigma}_f}{\bar{\varepsilon}_{c(a)}} \tag{B1}$$

where $\bar{\varepsilon}_{c(a)}$ is the average strain of the composite, $\bar{\sigma}_m$ is the average stress in the matrix, $\bar{\sigma}_f$ is the average stress in the fibre, and f_f is the volume fraction of the fibre. The average strain is

$$\bar{\varepsilon}_{c(a)} = f_f\frac{\bar{\sigma}_f}{E_f} + (1-f_f)\frac{\bar{\sigma}_m}{E_m} \tag{B2}$$

and the average stresses in both the matrix and fibre can be expressed as

$$\bar{\sigma}_m = \frac{2\pi\left\langle\left(\int_0^l\int_{r_1}^R r\sigma_m(x,r) + \int_l^L\int_0^{r_1} r\sigma_{ff}(x) + \int_l^L\int_{r_1}^R r\sigma_m(x,r)\right)\,\mathrm{d}r\,\mathrm{d}x\right\rangle}{(L-l)R^2\pi + l\pi(R^2-r_1^2)} \tag{B3}$$

$$\bar{\sigma}_f = \frac{2\pi}{\pi r_1^2 l}\int_0^l\int_0^{r_1} r\sigma_f(x)\,\mathrm{d}r\,\mathrm{d}x \tag{B4}$$

The first integral in Eq. (B3) represents the total stress acting in a volume equal to $l\pi(R^2-r_1^2)$; the two second integrals represents the total stress acting in a volume equal to $(L-l)\pi R^2$. The stresses $\sigma_f(x)$ and $\sigma_{ff}(x)$ are given by Eqs. (1) and (3), respectively. The function $\sigma_m(x,r)$ in Eq. (B3) describes the variation of the stress in the matrix. However, there is no need to know the explicit form of this function, since it can be eliminated by using the equilibrium condition expressed in Eq. (A1). The combination of Eqs. (A1) and (B3), yields

$$\bar{\sigma}_m = \frac{2\pi\left\langle\int_0^l\left(\frac{R^2\sigma_a}{2} - \int_0^{r_1} r\sigma_f(x)\,\mathrm{d}r\right)\,\mathrm{d}x + \int_l^L\int_0^{r_1} r\sigma_{ff}(x)\,\mathrm{d}r\,\mathrm{d}x + \int_l^L\left(\frac{R^2\sigma_a}{2} - \int_0^{r_1} r\sigma_f(x)\,\mathrm{d}r\right)\,\mathrm{d}x\right\rangle}{(L-l)R^2\pi + l\pi(R^2-r_1^2)} \tag{B5}$$

Finally, combining Eqs. (B2), (B4), and (B5), and substituting into Eq. (B1), the Young's modulus of the composite can be calculated.

(b) The fundamental equation in this approach is the usual relation

$$E_c = \frac{\sigma_a}{\bar{\varepsilon}_{c(b)}} \tag{B6}$$

where σ_a is the stress applied to the unit cell, and $\bar{\varepsilon}_{c(b)}$ is the average strain of the composite, here expressed as (Hsueh, 2000):

$$\bar{\varepsilon}_{c(b)} = \frac{w_o}{L} \tag{B7}$$

where L is the length of the unit cell (see Fig. 1) and w_o is the average displacement at $x = L$. The value of L and R as a function of the volume fraction of the fibre is calculated as (Hsueh, 2000):

$$L = l f_f^{2p-1}; \quad R = r f_f^{-p}; \quad p = \frac{1}{2} - \frac{1}{6}\exp\left(\frac{-l}{5r_1}\right) \tag{B8}$$

The average displacement at $x = l$ can be expressed as

$$w_l = \frac{2}{R^2}\left(\int_0^l\int_0^{r_1} r\frac{\sigma_f(x)}{E_f} + \int_0^l\int_{r_1}^R r\frac{\sigma_m(x,r)}{E_m}\right)\,\mathrm{d}r\,\mathrm{d}x \tag{B9}$$

Similarly, the average displacement at $x = L$ relative to $x = l$ is

$$w_L = \frac{2}{R^2}\left(\int_l^L\int_0^{r_1} r\frac{\sigma_{ff}(x)}{E_m} + \int_l^L\int_{r_1}^R r\frac{\sigma_m(x,r)}{E_m}\right)\times\mathrm{d}r\,\mathrm{d}x = \frac{(L-l)\sigma_a}{E_m} \tag{B10}$$

Again, the explicit formulation of the stress in the matrix $\sigma_m(x,r)$ is not required, since it can be eliminated by using Eq. (A1). The total displacement of the unit cell w_o is the sum of Eqs. (B9) and (B10). Therefore, combining Eqs. (B7), (B9), (B10), (1) and (3), and

substituting them into Eq. (B6), we finally obtain the expression for the Young's modulus of the composite as

$$E_c = L\sigma_a \left\langle \frac{L\sigma_a}{E_m} + \left(\frac{2A\sinh(\beta l)}{\beta} + \frac{lR^2 E_f \sigma_a}{S} \right) \times \left(\frac{1}{E_f} - \frac{1}{E_m} \right) \frac{r_1^2}{R^2} \right\rangle^{-1} \quad \text{(B11)}$$

where S, β, and A are given by Eqs. (A15), (A17) and (7), respectively.

References

Afonso, J.C., Ranalli, G., 2004. Crustal and mantle strengths in continental lithosphere: is the jelly sandwich model obsolete? Tectonophysics. 394, 221–232.

Aizawa, Y., Kazuhiko, I., Tatsumi, Y., 2001. Experimental determination of compressional wave velocities of olivine aggregates up to 1000 °C at 1 GPa. Tectonophysics 339, 473–478.

Anderson, D.L., 1988. Temperature and pressure derivatives of elastic constants with application to the mantle. J. Geophys. Res. 93, 4688–4700.

Anderson, O.L., Oda, H., Isaak, D., 1992. A model for the computation of thermal expansivity at high compression and high temperatures: MgO as an example. Geophys. Res. Lett. 19, 1987–1990.

Ansorge, J., Blundell, D., Mueller, S., 1992. Europe's lithosphere—seismic structure. In: Ansorge, J., Blundell, D., Mueller, S. (Eds.), A Continent Revealed. The European Geotraverse. European Science Foundation, Cambridge University Press, Cambridge, pp. 33–69.

Artemieva, I.M., Mooney, W.D., 2001. Thermal thickness and evolution of Precambrian lithosphere: a global study. J. Geophys. Res. 106, 16387–16414.

Artemieva, I.M., Billien, M., Lévêque, J.J., Mooney, W.D., 2004. Shear wave velocity, seismic attenuation, and thermal structure of the continental upper mantle. Geophys. J. Int. 157, 607–628.

Baker, M.B., Beckett, J.R., 1999. The origin of abyssal peridotites: a reinterpretation of constraints based on primary bulk compositions. Earth Planet. Sci. Lett. 171, 49–61.

Balling, N., 1995. Heat flow and thermal structure of the lithosphere across the Baltic Shield and northern Tornquist zone. Tectonophysics 244, 13–50.

Bass, J.D., 1995. Elasticity of minerals, glasses, and melts. In: Ahrens, T.J. (Ed.), Mineral Physics & Crystallography: A Handbook of Physical Constants, vol. 2. AGU Reference Shelf, pp. 45–63.

Bolton, H., Masters, G., 2001. Travel times of P and S from the global digital seismicnetworks: implications for the relative variation of P and S velocity in the mantle. J. Geophys. Res. 106, 13527–13540.

Boyd, F.R., 1989. Compositional distinction between oceanic and cratonic lithosphere. Earth Planet. Sci. Lett. 96, 15–26.

Canales, J.P., Detrick, R.S., Bazin, S., Harding, A.J., Orcutt, J.A., 1998. Off-axis crustal thickness across and along the East Pacific rise within the MELT area. Science 280, 1218–1221.

Čermák, V., Balling, N., Kukkonen, I., Zui, V.I., 1993. Heat flow in the Baltic Shield—results of the lithospheric geothermal modelling. Precambrian Res. 64, 53–65.

Chopelas, A., 2000. Thermal expansivity of mantle relevant magnesium silicates derived from vibrational spectroscopy at high pressure. Am. Miner. 85, 270–278.

Christensen, N.I., 1979. Compressional wave velocities in rocks at high temperature and pressures, critical thermal gradients, and crustal low-velocity zones. J. Geophys. Res. 84, 6849–6857.

Clyne, T.W., 1989. A simple development of the shear lag theory appropriate for composites with a relatively small modulus mismatch. Mater. Sci. Eng. 122, 183–192.

Cox, H.L., 1952. The elasticity and strength of paper and other fibrous materials. Br. J. Appl. Phys. 3, 72–79.

Dick, H.J.B., Fisher, R.L., Bryan, W.B., 1984. Mineralogic variability of the uppermost mantle along mid-ocean ridges. Earth Planet. Sci. Lett. 69, 88–106.

Doin, M.P., Fleitout, L., 1996. Thermal evolution of the oceanic lithosphere: an alternative view. Earth Planet. Sci. Lett. 142, 121–136.

Dziewonski, A.M., Anderson, D.L., 1981. Preliminary reference earth model. Phys. Earth. Planet. Int. 25, 297–356.

Everett, P.K., Arsenault, R.J., 1991. Metal Matrix Composites: Mechanisms and Properties. Academic Press, pp. 329–355.

Fei, Y., 1995. Thermal expansion. In: Ahrens, T.J. (Ed.), Mineral Physics, Crystallography: A Handbook of Physical Constants, vol. 2. AGU Reference Shelf, pp. 283–291.

Fernàndez, M., Torné, M., García-Castellanos, D., Vergés, J., Wheeler, W., Karpuz, R., 2004. Deep structure of the Vøring Margin: the transition from a continental shield to a young oceanic lithosphere. Earth Planet. Sci. Lett. 221, 131–144.

Fujisawa, H., 1998. Elastic wave velocities of forsterite and its β-spinel form and chemical boundary hypothesis for the 410-km discontinuity. J. Geophys. Res. 103, 9591–9608.

Gaul, O.F., Griffin, W.L., O'Reilly, S.Y., Pearson, N.J., 2000. Mapping olivine composition in the lithospheric mantle. Earth Planet. Sci. Lett. 182, 223–235.

Grad, M., Keller, G.R., Thybo, H., Guterch, A., POLONAISE Working Group, 2002. Lower lithospheric structure beneath the Trans-European Suture Zone from POLONAISE'97 seismic profiles. Tectonophysics 360, 153–168.

Gribb, T.T., Cooper, R.F., 1998. Low-frequency shear attenuation in polycrystalline olivine: grain boundary diffusion and the physical significance of the Andrade model for viscoelastic rheology. J. Geophys. Res. 103, 27267–27279.

Griffin, W.L., Ryan, C.G., Kaminsky, F.V., O'Reilly, S.Y., Natapov, L.M., Win, T.T., Kinny, P.D., Ilupin, I.P., 1999. The Siberian lithosphere traverse: mantle terranes and the assembly of the Siberian Craton. Tectonophysics 310, 1–35.

Hahn, T.A., 1991. Thermal expansion of metal matrix composites. In: Everett, P.K., Arsenault, R.J. (Eds.), Metal Matrix Composites: Mechanisms and Properties. Academic Press, pp. 329–355.

Hansen, U., Yuen, D.A., Kroening, S.E., Larsen, T.B., 1993. Dynamical consequences of depth-dependent thermal expansivity

and viscosity on mantle circulations and thermal structure. Phys. Earth Planet. Int. 77, 205–223.
Hawkesworth, C.J., Pearson, D.G., Turner, S.P., 1999. Chemical and temporal variations in the Earth's lithosphere. Phil. Trans. Roy. Soc., London A 357, 647–669.
Hill, R., 1952. The elastic behavior of a crystalline aggregate. Proc. Roy. Soc., London Ser. A 65, 349–354.
Hirth, G., Kohlstedt, D.L., 1996. Water in the oceanic upper mantle: implications for rheology, melt extraction and the evolution of the lithosphere. Earth Planet. Sci. Lett. 144, 93–108.
Hsueh, C.-H., 1995. A modified analysis for stress transfer in fibre-reinforced composites with bonded fibre ends. J. Mater. Sci. 30, 219–224.
Hsueh, C.-H., 2000. Young's modulus of unidirectional discontinuous-fibre composites. Compos. Sci. Technol. 60, 2671–2680.
Hull, D., Clyne, T.W., 1996. An Introduction to Composite Materials, 2nd ed. Cambridge University Press, UK, p. 326.
Jackson, I., Fitz Gerald, J.D., Faul, U.H., Tan, B.H., 2002. Grain-size-sensitive seismic wave attenuation in polycrystalline olivine. J. Geophys. Res. 107. NO.B12, 1360. doi:10.1029/2001JB001225.
Ji, S., Wang, Z., 1999. Elastic properties of forsterite–enstatite composites up to 3.0 GPa. J. Geodyn. 28, 147–174.
Ji, S., Wang, Q., Xia, B., 2002. Handbook of Seismic Properties of Minerals, Rocks and Ores. Polytechnic International Press, Montreal, p. 630.
Ji, S., Wang, Q., Xia, B., 2003. P-wave velocities of polymineralic rocks: comparison of theory and experiment and test of elastic mixture rules. Tectonophysics 366, 165–185.
Jing, Z.-C., Ning, J.-Y., Wang, S.-G., Zang, S.-X., 2002. Dynamic phase boundaries of olivine-wadsleyite in subduction zones in the western Pacific. Geophys. Res. Lett. 29 (22), 2045. doi:10.1029/2001GL013810.
Kanamori, H., Anderson, D.L., 1977. Importance of physical dispersion in surface wave and free oscillation problems: review. Rev. Geophys. Space Phys. 15, 105–112.
Karato, S.I., 1993. Importance of anelasticity in the interpretation of seismic tomography. Geophys. Res. Lett. 20, 1623–1626.
Ketcham, R.A., Beam, E.C., Kominz, M.A., 1995. Effects of temperature-dependent material properties and radioactive heat production on simple basin subsidence models. Earth Planet. Sci. Lett. 130, 31–44.
Klemme, S., O'Neill, H.Stc., 2000. The near-solidus transition from garnet lherzolite to spinel lherzolite. Contrib. Miner. Petrol. 138, 237–248.
Knittle, E., 1995. Static compression measurements of equations of state. In: Ahrens, T.J. (Ed.), Mineral Physics, Crystallography: A Handbook of Physical Constants, vol. 2. AGU Reference Shelf, pp. 98–142.
Kozlovskaya, E., Taran, L.N., Yliniemi, J., Giese, R., Karatayev, G.I., 2002. Deep structure of the crust along the Fennoscandia–Sarmantia Junction Zone (central Belarus): results of a geophysical–geological integration. Tectonophysics 358, 97–120.
Kreyszig, E., 1988. Advanced Engineering Mathematics. Wiley, New York, p. 1294.
Lay, T., Wallace, T.C., 1995. Modern Global Seismology. Academic Press, San Diego, p. 521.
Levshin, A.L., Ritzwoller, M.H., Barmin, M.P., Villaseñor, A., Padgett, C.A., 2001. New constraints on the arctic crust and uppermost mantle: surface wave group velocities, Pn, and Sn. Phys. Earth Planet. Int. 123, 185–204.
Li, G., Zhao, Y., Pang, S.-S., 1999. Four-phase sphere modelling of effective bulk modulus of concrete. Cement Concrete Res. 29, 839–845.
Lowrie, W., 1997. Fundamentals of Geophysics. Cambridge University Press, UK, p. 354.
Minster, J.B., Anderson, D.L., 1981. A model of dislocation-controlled rheology for the mantle. Phil. Trans. Roy. Soc. London 299, 319–356.
Nair, S.V., Kim, H.G., 1992. Modification of the shear lag analysis for determination of elastic modulus of short-fiber (or Whisker) reinforced metal matrix composites. J. Appl. Mech. 59, 176–182.
Nardone, V.C., 1987. Assessment of models used to predict the strength of discontinuous silicon carbide reinforced aluminium alloys. Scripta Metall. 21, 1313–1318.
Németh, B., Hajnal, Z., 1998. Structure of the lithospheric mantle beneath the trans-Hudson orogen, Canada. Tectonophysics 288, 93–104.
Niu, Y., Langmuir, C.H., Kinzler, R.J., 1997. The origin of abyssal peridotites: a new perspective. Earth Planet. Sci. Lett. 152, 251–265.
Niu, Y., O'Hara, M.J., Pearce, J.A., 2003. Initiation of subduction zones as a consequence of lateral compositional buoyancy contrast within the lithosphere: a petrological perspective. J. Petrol. 44, 851–866.
O'Reilly, S.Y., Griffin, W.L., Poudjom Djomani, Y.H., Morgan, P., 2001. Are lithospheres forever? Tracking changes in subcontinental lithospheric mantle through time. GSA Today 11, 4–10.
Parsons, B., Sclater, J.G., 1977. An analysis of the variation of the ocean floor bathymetry and heat flow with age. J. Geophys. Res. 82, 803–827.
Pearson, D.G., Boyd, F.R., Hoal, K.E.O., Hoal, B.G., Nixon, P.H., Rogers, N.W., 1994. A Re-Os isotopic and petrological study of Namibian Peridotites: contrasting petrogenesis and composition of on- and off-craton lithospheric mantle. Miner. Mag. 58, 703–704.
Peccerillo, A., Panza, G.F., 1999. Upper mantle domains beneath Central-Southern Italy: petrological, geochemical and geophysical constraints. Pure Appl. Geophys. 156, 421–443.
Poirier, J.P., Tarantola, A., 1998. A logarithmic equation of state. Phys. Earth Planet. Int. 109, 1–8.
Presnall, D.C., Gudfinnsson, G.H., Walter, M.J., 2002. Generation of mid-ocean ridge basalts at pressures from 1 to 7 GPa. Geochim. Cosmochim. Acta 66, 2073–2090.
Ravichandran, K.S., 1994. Elastic properties of two-phase composites. J. Am. Ceram. Soc. 77, 1178–1184.
Reynard, B., Price, G.D., 1990. Thermal expansion of mantle minerals at high pressures: a theoretical study. Geophys. Res. Lett. 17, 689–692.
Ritsema, J., van Heijst, H., 2000. New seismic model of the upper mantle beneath Africa. Geology 28, 63–66.
Robinson, J.A.C., Wood, B.J., 1998. The depth of the spinel to garnet transition at the peridotite solidus. Earth Planet. Sci. Lett. 164, 277–284.

Rudnick, R.L., McDonough, W.F., O'Connell, R.J., 1998. Thermal structure, thickness and composition of continental lithosphere. Chem. Geol. 145, 395–411.

Saxena, S.K., Shen, G., 1992. Assessed data on heat capacity, thermal expansion and compressibility for some oxides and silicates. J. Geophys. Res. B 97, 19813–19825.

Schmeling, H., Marquart, G., Ruedas, T., 2003. Pressure- and temperature-dependent thermal expansivity and the effect on mantle convection and surface observables. Geophys. J. Int. 154, 224–229.

Schubert, G., Turcotte, D.L., Olson, P., 2001. Mantle Convection in the Earth and Planets. Cambridge University Press, UK, p. 940.

Skirl, S., Hoffman, M., Bowman, K., Wiederhorn, S., Rödel, J., 1998. Thermal expansion behavior and macrostrain of Al_2O_3/Al composites with interpenetrating networks. Acta Mater. 46, 2493–2499.

Stacey, F.D., 1992. Physics of the Earth, 3rd ed. Brookfield Press, Brisbane, p. 513.

Starink, M.J., Syngellakis, S., 1999. Shear lag models for discontinuous composites: fibre end stresses and weak interface layers. Mater. Sci. Eng. A 270, 270–277.

Stein, C.A., Stein, S., 1992. A model for the global variation in oceanic depth and heat flow with lithospheric age. Nature 359, 123–128.

Suzuki, A., Ohtani, E., Kato, T., 1998. Density and thermal expansion of a peridotite melt at high pressure. Phys. Earth Planet. Int. 107, 53–61.

Vasco, D.W., Johnson, L.R., Marques, O., 2003. Resolution, uncertainty, and whole Earth tomography. J. Geophys. Res. 108, NO. B1, 2022. doi:10.1029/2001JB000412.

Villaseñor, A., Ritzwoller, M.H., Levshin, A.L., Barmin, M.P., Engdahl, E.R., Spakman, W., Trampert, J., 2001. Shear velocity structure of central Eurasia from inversion of surface wave velocities. Phys. Earth Planet. Int. 123, 169–184.

Wang, W., Takahashi, E., Sueno, S., 1998. Geochemical properties of lithospheric mantle beneath the Sino-Korea craton; evidence from garnet xenocrysts and diamond inclusions. Phys. Earth Planet. Int. 107, 249–260.

Watt, J.P., O'Connell, R.J., 1980. An experimental investigation of the Hashin-Shtrikman bounds on the two-phase aggregate elastic properties. Phys. Earth Planet. Int. 21, 359–370.

Yoda, S., Kurihara, N., Wakashima, K., Umekawa, S., 1978. Thermal cycling-induced deformation of fibrous composites with particular reference to the tungsten–copper system. Metall. Trans. A 9, 1229–1236.

Yu, J.-H., O'Reilly, S., Griffin, W.L., Xu, X., Zhang, M., Zhou, X., 2003. The thermal state and composition of the lithospheric mantle beneath the Leizhou Peninsula, South China. J. Volcanol. Geotherm. Res. 122, 165–189.

Zeyen, H., Dérerová, J., Bielik, M., 2002. Determination of the continental lithospheric thermal structure in the Western Carpathians: integrated modelling of surface heat flow, gravity anomalies and topography. Phys. Earth Planet. Int. 134, 89–104.

Zha, C.S., Duffy, T.S., Downs, R.T., Mao, H.K., Hemley, R.J., Weidner, D.J., 1998. Single-crystal elasticity of the α and β Mg_2SiO_4 polymorphs at high pressure. In: Manghnani, M.H., Yagi, T. (Eds.), Properties of Earth and Planetary Materials at High Pressure and Temperature, Monograph 101. AGU, pp. 9–16.

Zhao, P., Ji, S., 1997. Refinements of the shear-lag model and its applications. Tectonophysics 279, 37–53.

Zheng, J., O'Reilly, S.Y., Griffin, W.L., Lu, F., Zhang, M., Pearson, N.J., 2001. Relict refractory mantle beneath the eastern North China block: significance for the lithosphere evolution. Lithos 57, 43–66.

Zhou, H., 1996. A high-resolution P wave model for the top 100 km of the mantle. J. Geophys. Res. 101, 27791–27810.